

AD-A017 873

STATIC-ELECTRICITY ANALYSIS PROGRAM. VOLUME I

Joseph E. Nanevich, et al

Stanford Research Institute

Prepared for:

Space and Missile Systems Organization

October 1974

DISTRIBUTED BY:

**NTIS**

National Technical Information Service  
U. S. DEPARTMENT OF COMMERCE

339094

SAMSO TR 75-44

*Final Report — Volume I*

*October 1974*

ADA 017873

## STATIC-ELECTRICITY ANALYSIS PROGRAM

By: J. E. NANEVICZ      D. G. DOUGLAS

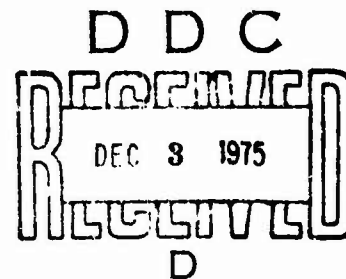
*Prepared for:*

DEPARTMENT OF THE AIR FORCE  
HQ SPACE & MISSILE SYSTEMS ORGANIZATION (AFSC)  
P.O. BOX 92960  
WORLDWAY POSTAL CENTER  
LOS ANGELES, CALIFORNIA 90009

CONTRACT F04701-73-C-0401

Approved for public release; distribution unlimited.

SRI Project 2919



**STANFORD RESEARCH INSTITUTE**  
Menlo Park, California 94025 · U.S.A.

Reproduced by  
NATIONAL TECHNICAL  
INFORMATION SERVICE  
U.S. Department of Commerce  
Springfield, VA. 22151

Copy No. 74

REPORT DOCUMENTATION PAGE		READ INSTRUCTIONS BEFORE COMPLETING FORM	
1. REPORT NUMBER SAMSO TR 75-44 Volume I	2. GOVT ACCESSION NO.	3. RECIPIENT'S CATALOG NUMBER	
4. TITLE (and Subtitle) STATIC-ELECTRICITY ANALYSIS PROGRAM Volume I		5. TYPE OF REPORT & PERIOD COVERED Final Report--Volume I Covering the Period Sept. 1973 to August 1974	
		6. PERFORMING ORG. REPORT NUMBER SRI Project 2919	
7. AUTHOR(s) Joseph E. Nanevicz Dennis G. Douglas		8. CONTRACT OR GRANT NUMBER(s) Contract F04701-73-C-0401	
		10. PROGRAM ELEMENT, PROJECT, TASK AREA & WORK UNIT NUMBERS	
9. PERFORMING ORGANIZATION NAME AND ADDRESS Stanford Research Institute Menlo Park, California 94025		12. REPORT DATE October 1974	13. NO. OF PAGES 91
11. CONTROLLING OFFICE NAME AND ADDRESS Department of the Air Force HQ Space & Missile Systems Organization (AFSC) P. O. Box 92960, Worldway Postal Center Los Angeles, California 90009		15. SECURITY CLASS. (of this report) UNCLASSIFIED	
14. MONITORING AGENCY NAME & ADDRESS (if diff. from Controlling Office)		15a. DECLASSIFICATION/DOWNGRADING SCHEDULE N/A	
16. DISTRIBUTION STATEMENT (of this report) Approved for public release; distribution unlimited.			
17. DISTRIBUTION STATEMENT (of the abstract entered in Block 20, if different from report)			
18. SUPPLEMENTARY NOTES			
19. KEY WORDS (Continue on reverse side if necessary and identify by block number) Static electrification                      Computer modeling Precipitation static                      Radio noise Aircraft Computer analysis			
20. ABSTRACT (Continue on reverse side if necessary and identify by block number) <p>A computer program based on the results of earlier experimental and analytical studies of precipitation static interference was developed to permit the EMP engineer to calculate p-static noise levels on a variety of aircraft under various charging conditions.</p> <p>The experimental and analytical data on which the program is based are presented briefly. The approach and philosophy followed in preparing the computer</p> <p style="text-align: right;">(continued)</p>			

D D C  
RECEIVED  
DEC 3 1975  
RECEIVED  
D

19. KEY WORDS (Continued)

20 ABSTRACT (Continued)

model are discussed. Comparisons of predicted noise spectra to flight test data from a Boeing 707, an F-4, and a B-47 are given that verify the validity of the computer model.

A discussion is presented of the applications and limitations of this first-generation computer model.

CONTENTS

DD FORM 1473 . . . . . i

ILLUSTRATIONS . . . . . v

TABLE . . . . . vi

I INTRODUCTION . . . . . 1

    A. General . . . . . 1

    B. Scope of Present Program . . . . . 3

II PRECIPITATION CHARGING, NOISE GENERATION,  
AND COUPLING . . . . . 5

    A. General . . . . . 5

    B. Noise Sources . . . . . 5

        1. Corona Discharge . . . . . 5

        2. Streamer Discharge . . . . . 8

    C. Electromagnetic Coupling . . . . . 10

        1. General . . . . . 10

        2. KC-135 Corona Source Coupling . . . . . 11

            a. Measured Coupling Data . . . . . 11

            b. Effects of Antenna Size on Corona Noise  
                Coupling . . . . . 14

        3. Coupling to Streamer Sources . . . . . 15

    D. Equivalent Noise Field . . . . . 20

    E. Aircraft Charging . . . . . 22

        1. Total Aircraft Charging Current (Corona) . . . . . 22

        2. Localized Charging (Streamers) . . . . . 26

III COMPUTER MODELING OF EXISTING DATA . . . . . 29

    A. General . . . . . 29

    B. Corona Noise . . . . . 29

C.	Streamer Noise . . . . .	31
D.	Verification of Computer Model . . . . .	33
1.	General . . . . .	33
2.	Corona Noise . . . . .	34
a.	707 Belly Antenna . . . . .	34
b.	707 Tail Cap Antenna . . . . .	35
c.	F-4 Tail Cap Antenna . . . . .	37
d.	F-4 Belly Antenna . . . . .	41
3.	Streamer Noise . . . . .	41
a.	B-47 Coated Radome Antenna . . . . .	41
b.	B-47 Uncoated Radome Antenna . . . . .	44
IV	APPLICATION AND LIMITATIONS OF COMPUTER MODEL . . . . .	47
A.	General. . . . .	47
B.	Applications . . . . .	47
1.	Corona Noise . . . . .	47
2.	Streamer Noise . . . . .	49
C.	Limitations . . . . .	51
1.	Corona Noise . . . . .	51
2.	Streamer Noise . . . . .	52
V	CONCLUSIONS AND RECOMMENDATIONS . . . . .	53
APPENDICES		
A.	STREAMER DISCHARGE CHARACTERISTICS . . . . .	57
B.	METHOD-OF-MOMENTS CALCULATION OF COUPLING TO KC-135 TAIL-CAP . . . . .	77
ACKNOWLEDGMENTS	. . . . .	87
REFERENCES	. . . . .	89

## ILLUSTRATIONS

1	Frictional Charging of Aircraft by Impinging Particles . . . . .	1
2	Noise Sources Associated with Static Electrification . . . . .	2
3	Corona-Noise-Source Spectrum Characteristics. . . . .	7
4	Typical Current Pulses Induced by Streamer Discharges . . . . .	9
5	Antenna and Corona-Noise-Source Locations for KC-135 Coupling Measurements . . . . .	12
6	Measured Coupling Factors for Antennas on Boeing 367-80 Aircraft . . . . .	13
7	Variation, Near Wing-Tips of Coupling to Belly Antenna in KC-135 Aircraft . . . . .	14
8	Noise Coupling to Radome . . . . .	16
9	Noise Coupling to Canopy . . . . .	18
10	Calculated Values of Coupling Factor Compared to Values Measured by Field Probe . . . . .	19
11	Percent Intercept as a Function of Airfoil Size . . . . .	25
12	Corona-Noise Fields at 707 Belly Antenna . . . . .	34
13	Corona-Noise Fields at 707 Tail-Cap Antenna . . . . .	36
14	Predicted Corona-Discharge Noise Fields on 707 Tail-Cap Antenna in Frontal Snow . . . . .	38
15	Corona-Noise Fields at F-4 Tail-Cap Antenna . . . . .	40
16	Corona-Noise Fields at F-4 Chelton Antenna (Top of Fuselage) . . . . .	42
17	Noise Spectrum in Coated Radome Section on B-47 Aircraft . . . . .	43
18	Noise Spectrum in Uncoated Radome Antenna Section on B-47 Aircraft . . . . .	45
A-1	Dielectric Shapes and Antenna Arrangements for Which Streamer Statistical Calculations Were Carried Out . . . . .	62

A-2	Approximation to Region of Radome in Which Charging Occurred . . . . .	64
A-3	Variation of Coupling Factor with Distance from Radome Nose . . . . .	67
A-4	Rectangular Dielectric Region of Charging . . . . .	69
A-5	Streamer-Noise-Source Spectra for the Physical Configuration of Figure A-1. . . . .	74
A-6	Streamer-Noise-Source Spectra for Triangular Dielectric Regions . . . . .	75
A-7	Streamer-Noise-Source Spectra for Rectangular Dielectric Regions . . . . .	76
B-1	Cylindrical Element Approximation to KC-135 Aircraft . . . . .	80
B-2	Computed and Experimental Coupling Data . . . . .	82
B-3	Adjusted Calculations Compared to Measured Coupling Data . . . . .	83
B-4	Technique for Treating Joints in Method-of-Moments Calculation . . . . .	85

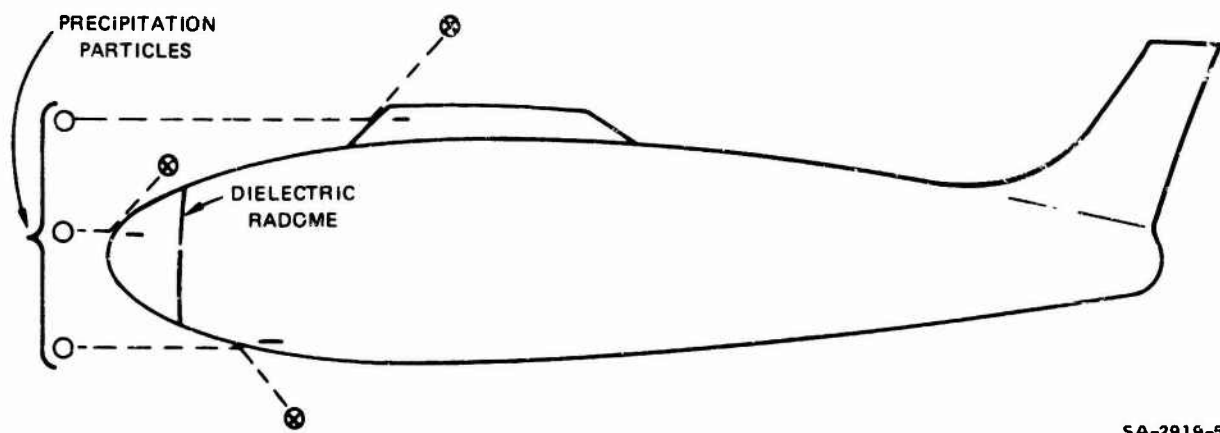
TABLE

A-1	Results of Streamer Statistical Calculations . . . . .	72
-----	--	----

## I INTRODUCTION

### A. General

When an aircraft or other flight vehicle is operated in precipitation containing ice crystals, frictional electrification associated with particle impact causes the impinging particles to acquire a net charge and to deposit an equal and opposite charge on the vehicle.<sup>1-5\*</sup> As shown in Figure 1, charging occurs on frontal metallic and dielectric portions of the vehicle.<sup>6,7</sup> Although the charge deposited by a single



SA-2919-5

FIGURE 1 FRICTIONAL CHARGING OF AIRCRAFT BY IMPINGING PARTICLES

crystal changes the potential of the aircraft only slightly (of the order of 0.01 volt change for the case of a KC-135 struck by a cirrus-cloud crystal<sup>4</sup>), the particle impact rate in a typical cloud is sufficient that the vehicle reaches a potential of hundreds of kilovolts in less than a second.<sup>4</sup>

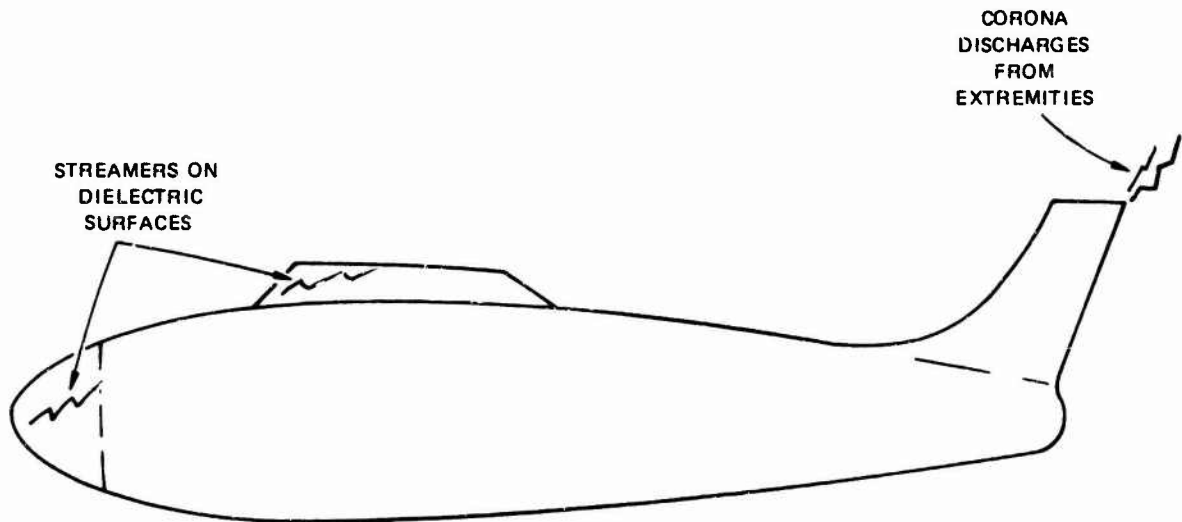
Charge deposited on dielectric surfaces such as the radome or canopy is bound there because these surfaces are insulators. As a

---

\*References are listed at the end of the report.

result, under precipitation charging conditions, it is possible for a potential difference of hundreds of kilovolts to exist between a dielectric surface and the surrounding airframe structure.

The electrification of the vehicle is of relatively little consequence in itself because the energies involved are small, and since the electrostatic fields do not penetrate to the interior. It is the consequences of the electrification (Figure 2) that are of concern. When the



SA-2919-6

FIGURE 2 NOISE SOURCES ASSOCIATED WITH STATIC ELECTRIFICATION

vehicle potential reaches roughly 100 kV, the electric field intensity at the aircraft extremities becomes sufficiently high that electrical breakdown of the air (corona discharge) occurs.<sup>8</sup> At aircraft operating altitudes, the corona breakdown from the extremities occurs not as a continuous flow of charge but as a series of pulses with roughly 10 ns rise time and 200 ns duration, and it therefore generates radio noise over a broad spectrum.<sup>4,5,8</sup>

A similar situation exists on the dielectric frontal surfaces. As charge continues to accumulate on the dielectric, the potential to the airframe rises until the electric-field intensity at the dielectric

surface becomes sufficiently high that voltage breakdown (streamer discharge) occurs across the plastic surface. A surface streamer involves the rapid transfer of charge over a substantial distance, and also generates serious radio frequency interference.<sup>6,7</sup>

The degree to which the radio frequency noise generated by corona and streamer discharges couples into electronic systems on the flight vehicle is determined by the relative locations of the noise source, and the "antenna" via which the noise is coupled into the affected system. In addition, the coupling depends on frequency, the size of the vehicle, and the size of the antenna.<sup>4,5,7</sup>

#### B. Scope of Present Program

On earlier programs, various aspects of the problem of precipitation-static noise generation and coupling were studied analytically and experimentally both in the laboratory and in flight tests. Although the earlier work was directed largely toward specific aircraft, the results are capable of being generalized and applied to similar vehicles. Unfortunately, the results are spread over a large number of reports, each of which treats a limited part of the overall problem. Thus, the EMC engineer is in the position of having to be familiar with all of the publications in considerable depth if he is to apply the results of the earlier work to his problems.

The purpose of the present program is to systematize the results of earlier precipitation-static studies, and to prepare mathematical models based on this earlier work to permit the results to be incorporated in the Air Force Intrasystem EMC Analysis Program currently under development.<sup>9</sup>

It was recognized at the outset that the scope of the program would be circumscribed by existing data on noise sources and coupling.

It was noted, however, that existing results could be applied to a considerable variety of situations, and that incorporating a precipitation-static model into the Intrasystem EMC Analysis Program at this time would be of considerable immediate benefit to the EMC engineer. Further refinements of the precipitation-static model can be accomplished as new experimental data become available and as new analytical techniques are developed.

In preparing the precipitation static model (available as Vol II of this report), one of the objectives was that it be compatible with the Air Force Intrasystem EMC Analysis Program (IAP). As work progressed, it was determined that the structure and functioning of the precipitation static model was such that it lent itself to embodiment as a "stand-alone" program. Since it appeared likely that there would be further refinement and development of the IAP, it was decided that the precipitation static model should indeed be generated in the form of a stand-alone program that can be called when needed. The outputs of the precipitation static model are values of precipitation static noise field intensity at selected locations on the aircraft. These form natural input data for the IAP.

## II PRECIPITATION CHARGING, NOISE GENERATION, AND COUPLING

### A. General

As indicated earlier, considerable work has been done on the investigation of precipitation-static noise generation and coupling processes. The essential results of this work will be presented here together with an indication of the special considerations or limitations that might apply to the result used. An effort will be made to avoid repeating derivations and analyses here. Instead, extensive reference will be made to the original work.

### B. Noise Sources

#### 1. Corona Discharge

In Ref. 8 it was shown that the individual pulses associated with a corona discharge can be well approximated by a decaying exponential with zero rise time, as follows:

$$f(t) = A e^{-\alpha t} \quad (1)$$

where  $A$  is the pulse amplitude and  $\alpha$  is the pulse decay constant. Both of these terms are functions of altitude. In Ref. 4 it is shown that the noise spectrum produced by  $\nu$  such pulses occurring each second is given by

$$P = A \left( \frac{\nu}{\pi} \right)^{\frac{1}{2}} \left( \omega^2 + \alpha^2 \right)^{-\frac{1}{2}} \quad (2)$$

Further experimental work described in Ref. 4 systematically explored the dependence of corona-discharge-noise characteristics on altitude. The results of this work shown in Figure 3 demonstrate that both the amplitude and spectral character of the noise are strongly altitude-dependent. In preparing Figure 3, curves of the form of Eq. (2) were plotted to fit the experimental data as well as possible.

Previous calculations of equivalent noise field relied on "look-up" and nomograph techniques to obtain P, the relative source-spectrum magnitude. An alternative and much better computer solution was found by defining a, v, and  $\alpha$  in terms of an analytical fit to the plotted data, which was a function of pressure.

It was determined that a good fit to A, v, and  $\alpha$  could be obtained by expressing

$$A = 7.90569 \times 10^5 p^{0.25} \quad (3)$$

$$v = 3.83767 \times 10^3 p^{0.48} \quad (4)$$

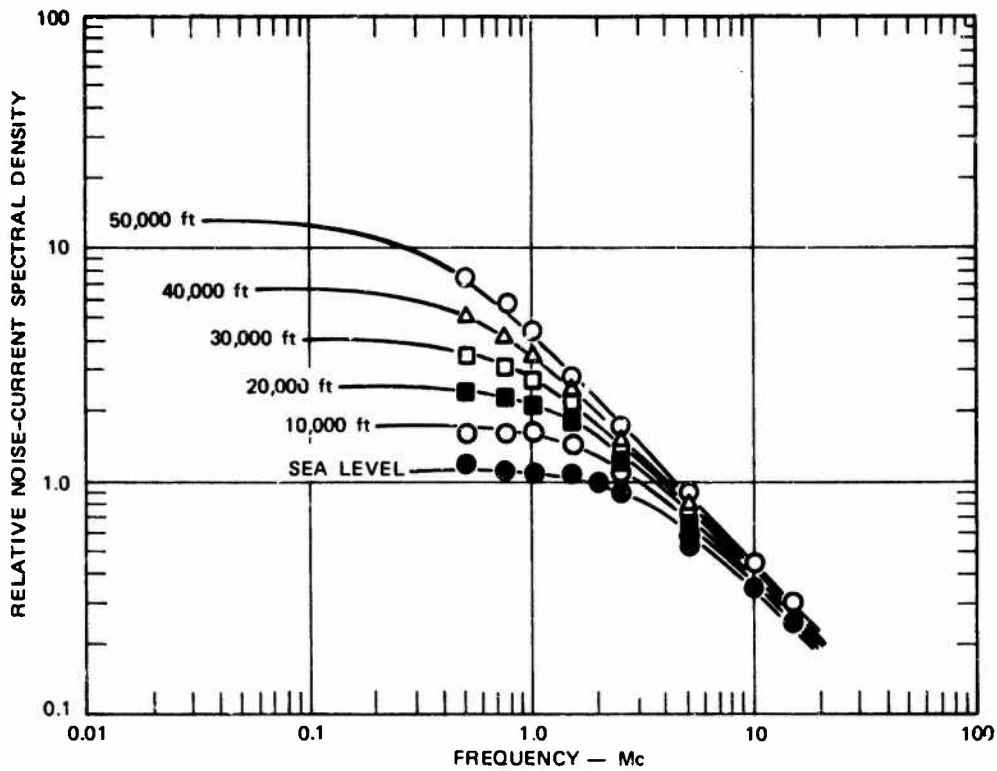
$$\alpha = 2.7777 \times 10^{-2} p \quad (5)$$

where p is in torr.

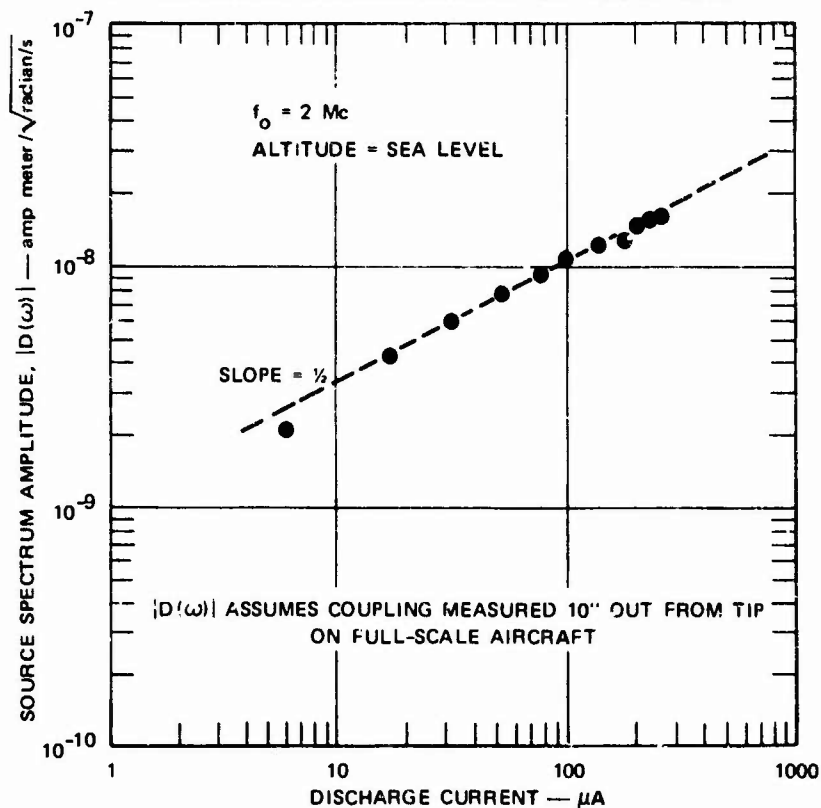
A fit to the 1962 U.S. Standard Atmosphere<sup>10</sup> resulted in the expression

$$p(\text{torr}) = 760 \exp \left( -\frac{h + 0.002 h^2}{25} \right) \quad (6)$$

where h is in kilofeet. Inserting Eq. (6) into Eqs. (3), (4), and (5) and inserting these in turn into Eq. (2) resulted in an expression for the relative source-spectrum amplitude that was uniquely determined by the altitude and frequency and is denoted by the variable name PREL in the program.



(a) NORMALIZED SPECTRUM SHOWING ALTITUDE EFFECTS



(b) RELATIONSHIP OF ABSOLUTE NOISE LEVEL TO DISCHARGE CURRENT

SA-2919-7

FIGURE 3 CORONA-NOISE-SOURCE SPECTRUM CHARACTERISTICS

## 2. Streamer Discharge

In the program of Refs. 6 and 7, flight-test and laboratory measurements were made of streamer discharge characteristics. In the work of Ref. 7, an analysis was made of the signals that streamers induce in receiving systems. Certain essentials of this analytical work are presented in Appendix A along with extensions and generalizations required for the present program.

The results of the streamer studies indicate that streamer discharges induce pulses of the sort shown in Figure 4, which illustrates the pulses generated in a wire located immediately below the dielectric surface on which streamers occur. It is evident from Figure 4 that the time waveform of the streamer pulse depends on the length of the streamer. The amplitude of the induced pulse, of course, depends on the coupling between the streamer and the receiving "antenna."

To define the noise spectrum generated by streamers occurring in a practical situation, it is necessary to derive a statistical description for a series of pulses such as those shown in Figure 4 occurring at random times with randomly varying amplitudes and time structures. Such statistical analyses were carried out in Appendix A for the three general arrangements of dielectric region and receiving antenna shown in Figure A-1. The results of the statistical analyses are given in Table A-1 and appear to be quite dissimilar. However, when the statistical results are used to calculate noise-source spectra as shown in Figure A-5, it is found that the resulting noise-source spectra generated on the various surfaces are virtually indistinguishable.

In a further exploration of streamer-noise-source characteristics, source-spectrum calculations were carried out for different sizes of the dielectric streamer-noise-source region (streamer discharge lengths varied). The results of these calculations indicate that

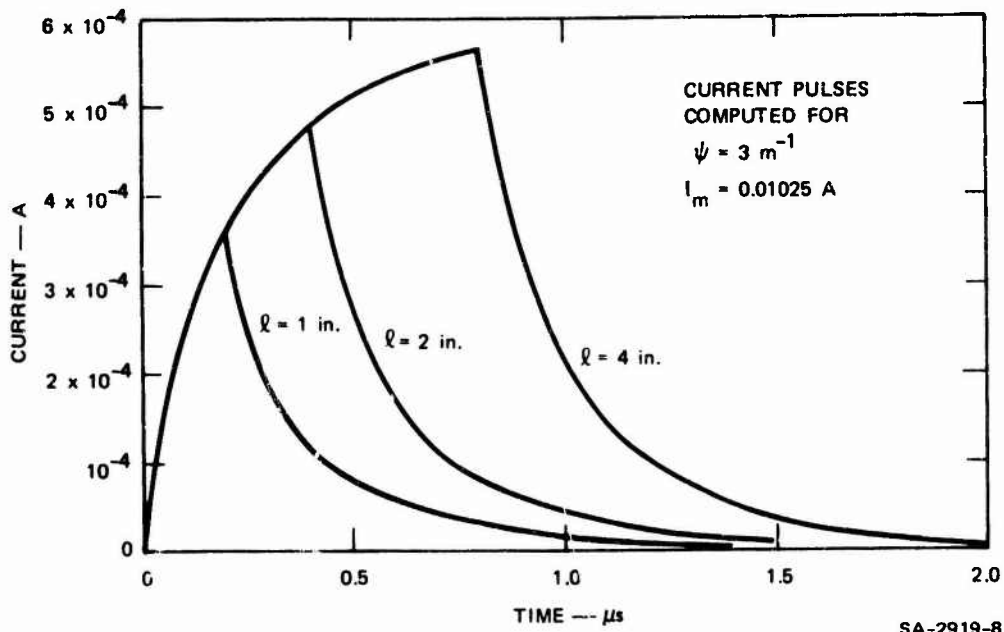


FIGURE 4 TYPICAL CURRENT PULSES INDUCED BY STREAMER DISCHARGES

increasing the size of the region has the effect of increasing the low-frequency content of the streamer-noise-source spectrum as shown in Figures A-6 and A-7.

Essentially the results given in Appendix A give expressions for streamer-noise-source spectra as a function of charging current for a number of representative geometrical arrangements of dielectric and antenna. Of particular interest in the results of Appendix A are the facts that source spectral characteristics depend primarily on the dimension of the longest streamer that can occur on the dielectric region, and that they do not depend critically on the shape of the dielectric region. This means that in the computer model it is not necessary to be precise about specifying the form of the region on which the streamer discharges occur.

## C. Electromagnetic Coupling

### 1. General

Simply specifying the spectral character of the noise source as was done in the previous sections is not sufficient to determine the noise experienced by a system. It is also necessary to specify the electromagnetic coupling between the noise source and the "antenna" of the affected system. Analytical determinations of coupling in simple physical structures were made in Ref. 8. An experimental technique for measuring coupling was developed in the program of Ref. 7, and used to study coupling between a streamer source and a nearby antenna. (In this case the dimensions of the coupling structure were small compared to the wavelength of signals of interest.) In the work of Ref. 4 the method was extended to the determination of the coupling between aircraft extremities where corona discharges occur, and receiving-antenna locations on the aircraft. (Here the dimensions of the structure were up to several wavelengths long at the frequencies of interest.) Further measurements were made<sup>11</sup> to determine the coupling between antennas mounted on the fuselage of an aircraft and streamers occurring on the radome or canopy.

The coupling-measurement technique has involved the use of an isolated broadband spark noise source positioned at the p-static source location, and either an oscilloscope or a radio receiver connected to the antenna in question. This measurement technique yields the magnitude of the coupling factor, but provides no information regarding phase. Using the coupling data, it is possible to specify the noise spectrum at an antenna location, but generally it is not possible to predict the time waveform of the noise pulses induced in the antenna terminals. To calculate time waveforms, it is necessary to know both the phase and amplitude of the coupling function. (In some special cases<sup>12</sup> it is

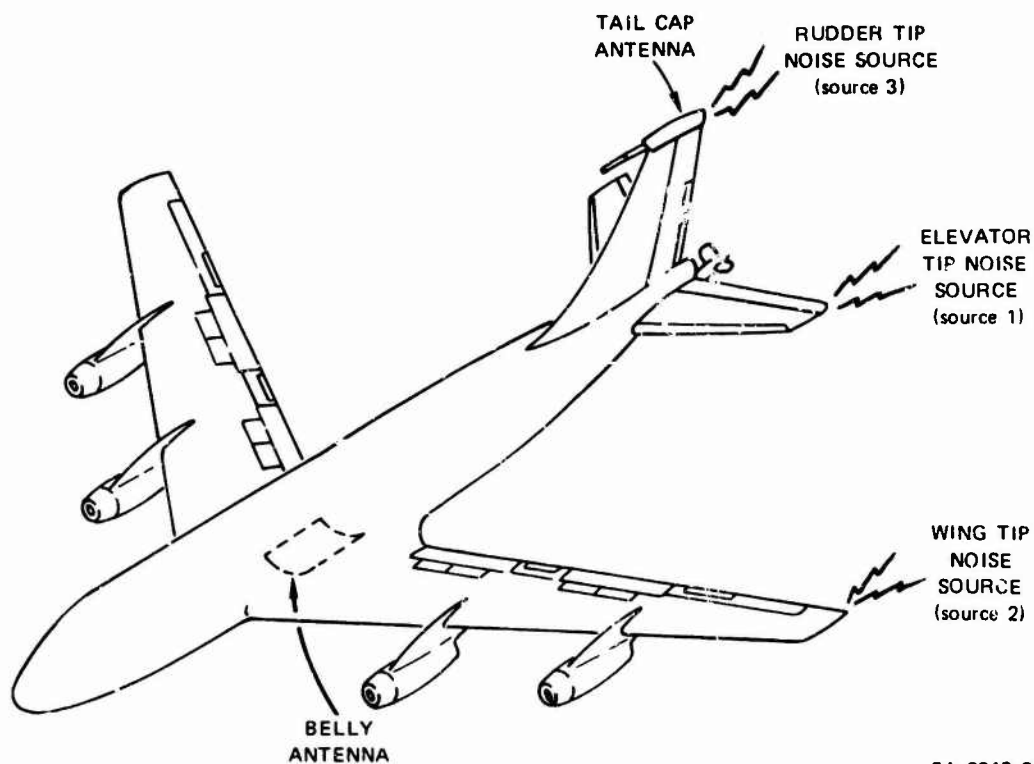
possible to use supplemental information and to synthesize an expression for the phase function. In general, however, the available coupling data do not allow pulse waveform prediction.)

It should be noted at this time that the systematic development of computer techniques such as the method of moments for the solution of electromagnetic problems offers the promise of providing information regarding both amplitude and phase of the coupling function. To investigate the utility of such techniques, a computer run was made using a program already available at SRI to calculate coupling fields at the extremities of a very crude cylinder model of a swept-wing aircraft. The results of this calculation presented in Appendix B are very encouraging, since the computer calculations are remarkably accurate in predicting the resonances and general behavior of the coupling functions. Since no effort was made to match the size of the "antenna" used in the computer calculations with that of an actual aircraft antenna, the magnitude of the calculated coupling could not be compared with measured values. There is no reason to expect that the magnitude cannot be predicted with accuracy.

## 2. KC-135 Corona Source Coupling

### a. Measured Coupling Data

The physical arrangement considered in the KC-135 noise-coupling measurements of Ref. 4 is shown in Figure 5. The antennas used in making the measurements were a small tail-cap and a flush belly antenna located in a fairing at the root of the wing. Coupling was measured between each of these antennas and the noise source regions at each of the airfoil extremities. The results of the measurements are shown in Figure 6.



SA-2919-9

FIGURE 5 ANTENNA AND CORONA-NOISE-SOURCE LOCATIONS FOR KC-135 COUPLING MEASUREMENTS

Although the coupling-measurement technique used inevitably includes the test-antenna characteristics in the measured results, the form of the coupling as a function of frequency will not be affected by the details of the test antenna, provided the antenna dimensions are small compared to a wavelength at the frequencies of interest. In this case, only the magnitude of the coupling function will be affected by a change in the antenna. The data shown in Figure 6 have therefore been adjusted to represent the coupling to an antenna having unity induction area,  $a$ , in response to a low-frequency, vertically polarized signal.

The variation with frequency of the coupling to the various points is of considerable interest, since it shows the effect of the various electromagnetic resonances of the aircraft. For example, the peak in coupling between the belly antenna and the tips of the tail surfaces at approximately 3 MHz occurs at the frequency that makes the

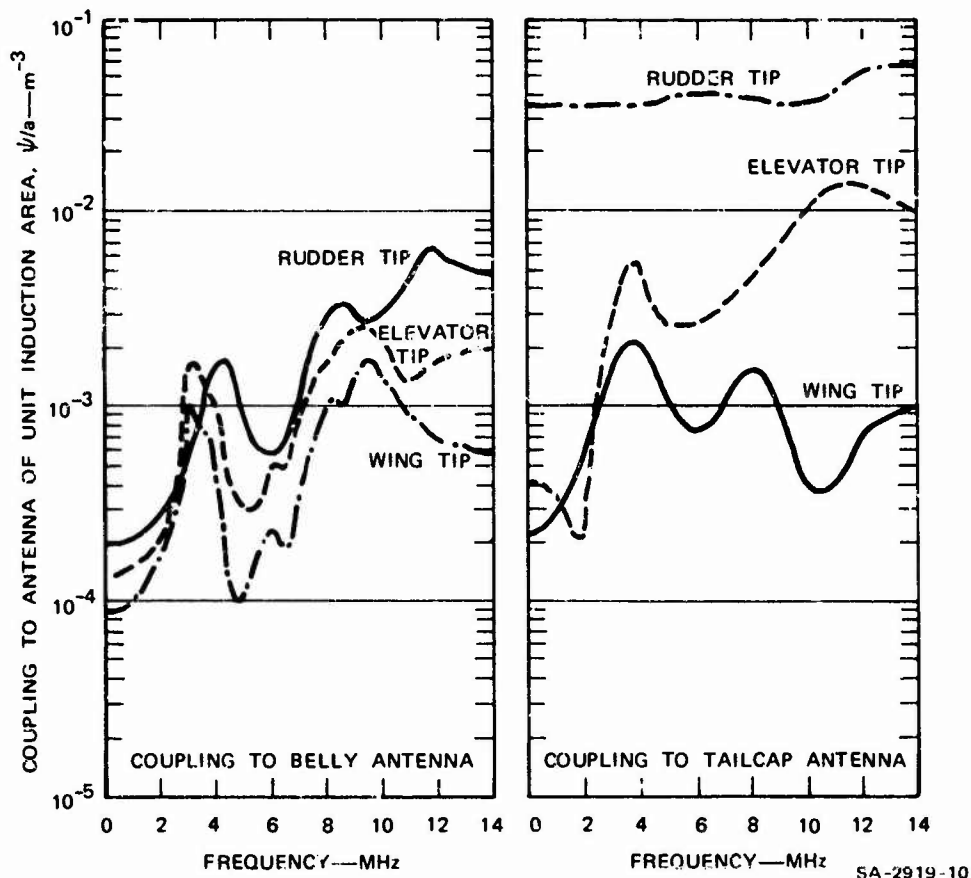
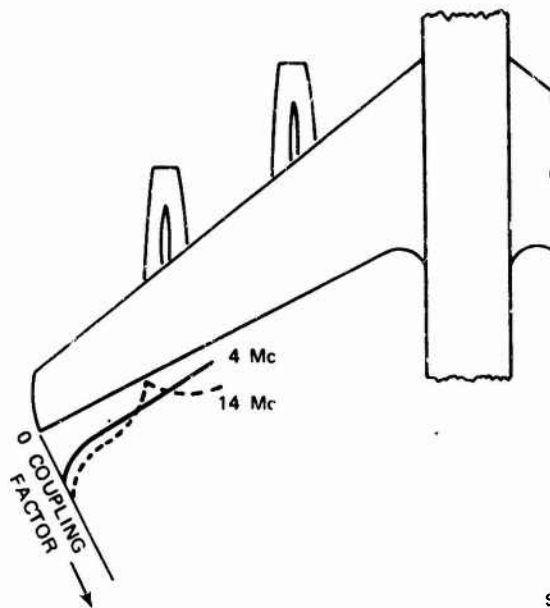


FIGURE 6 MEASURED COUPLING FACTORS FOR ANTENNAS ON BOEING 367-80 AIRCRAFT

path distance from a point just aft of the wings to a tip of one of the tail surfaces one-quarter wavelength. The presence of the resonance peaks in the coupling function serves to emphasize the fact that the pulses arriving at the antenna terminals will differ from the pulses generated by the corona discharges at the extremities in that they will be stretched out in time by aircraft resonances.<sup>12</sup>

Also of interest is the variation of the coupling at a particular frequency, with position along an airfoil. This is illustrated in Figure 7 which is a plot of the variation in coupling of the belly antenna to the trailing edge of the wing near the tip. The coupling is



SA-2919-11

FIGURE 7 VARIATION, NEAR WING-TIP, OF COUPLING TO BELLY ANTENNA IN KC-135 AIRCRAFT

proportional to the charge density that would be excited by the antennas if a voltage were applied to them. At all frequencies the charge tends to concentrate at the extremities, as shown by the plot in Figure 7. Thus, the coupling tends to be maximum at the points where discharges are most likely to occur. The dip in coupling at 14 MHz occurs at a distance approximately one-quarter wavelength from the tip. This result also indicates the fallacy in assuming that the noise induced in an antenna on an aircraft will always decrease as the noise source is moved away from the antenna. From Figure 7 it is apparent that on the trailing edge of the wing near the tip, moving a noise source away from the belly antenna increases the noise induced in the antenna.

b. Effects of Antenna Size on Corona Noise Coupling

The data of Figure 6 can be applied without restriction to aircraft of similar shape but different size. In general, the same resonances will occur on the scaled aircraft, but they will occur at

the scaled frequency. In Ref. 4 it is shown that on the scaled aircraft the coupling  $\psi_{1/n}$  (at the scaled frequency  $n\omega$ ) varies as the square root of the scale  $n$  of the aircraft ( $n > 1$ ). Thus,

$$\psi_{1/n} = \psi \sqrt{n} . \quad (7)$$

(The square root occurs as the result of an artifice in the way in which the absolute corona-noise-source level is defined.) In order for Eq. (7) to be valid everything about the general form of the aircraft (including antenna size) must be scaled. This means that the induction area,  $a$ , of the test antenna varies as the inverse square of the scale  $n$ , so that

$$a_{1/n} = a/n^2 . \quad (8)$$

Thus the normalized coupling on the  $1/n$ -scale aircraft varies as

$$\psi/a \Big|_{1/n} = n^{5/2} \psi/a . \quad (9)$$

### 3. Coupling to Streamer Sources

The spark noise-source technique was used in the work of Ref. 11 to measure the coupling between three antennas located on the fuselage of an aircraft, and the surface of a radome located on the nose. The measurements were made using an oscilloscope connected to the antenna terminals, and represent the low-frequency coupling, which is of primary interest because streamer noise spectra fall off rapidly with increasing frequency above 1 MHz. The results of these measurements are reproduced in Figure 8.

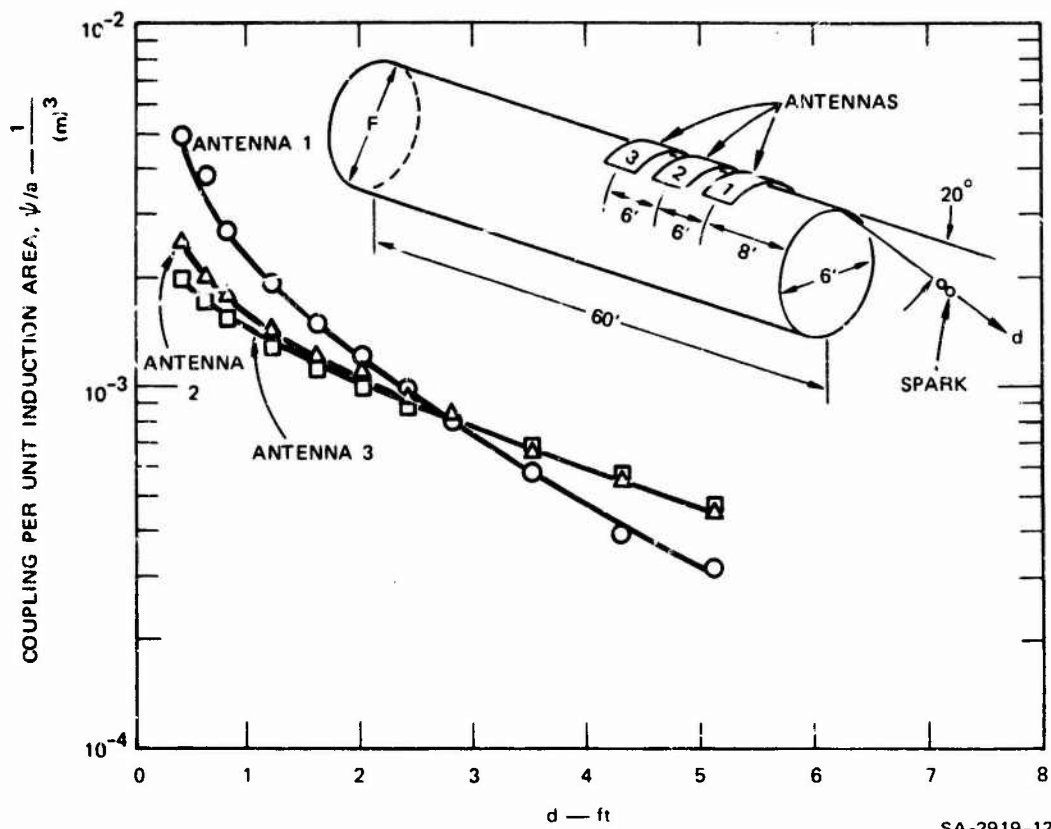


FIGURE 8 NOISE COUPLING TO RADOME

One of the most striking features evident in the coupling data of Figure 8 is the fact that the coupling is relatively independent of antenna location on the fuselage. This result is in keeping with the work in Chapter VII of Ref. 4 where it is shown that, for the case of a cylindrical structure with a noise source at one end, the electric noise field intensity under quasi static conditions (noise coupling) is independent of position along the cylinder [see Eq. (61), Ref. 4]. Also, the work of Ref. 4 indicates that the magnitude of the electric field is inversely proportional to the peripheral distance around the cylinder. This relationship is useful in applying the data of Figure 8 to aircraft of different size. It may also be used to treat antennas located on a tapered section of the aircraft such as the nose.

It is interesting to note from Figure 8 that the magnitude of the coupling from the fuselage antennas to the radome is of the same order as the coupling of the belly antenna to the airfoil extremities. Also, we should note that the source intensity (at low frequencies) for streamer discharges is roughly the same as for corona for a given discharge current. It should be observed, however, that all of the current arriving on a vehicle is discharged as corona, whereas only a small fraction of the total charging current (that arriving on the dielectric surface in question) contributes to the streamer-noise-generation process. Thus, except for antennas located in the immediate vicinity of a frontal dielectric surface (in which case coupling is high), streamer noise is generally less of a problem than corona noise.

Also in the program of Ref. 11, measurements were made of the coupling between antennas located on the fuselage of an aircraft and streamers occurring on a canopy structure over the antenna region. The results of these measurements are shown in Figure 9. It is evident that in this arrangement, the coupling is highly dependent on the antenna involved. In the case of the forward antenna the coupling is particularly high, so that an antenna in this location relative to the canopy would be strongly affected by streamers occurring on the canopy surface. It is also interesting to notice that the coupling in Figure 9 is relatively independent of the position of the streamer discharge on the canopy.

Reference 7 describes a study of streamer coupling to "antennas" located on the back surface of the dielectric on which streamers were occurring. First, consideration was given to the idealized geometry of Figure 10, which also allows analytical solution, and which therefore also permitted evaluation of the spark-discharge-probe coupling-measurement technique. This configuration may be considered representative of the practical case of an antenna wire mounted on the back of a

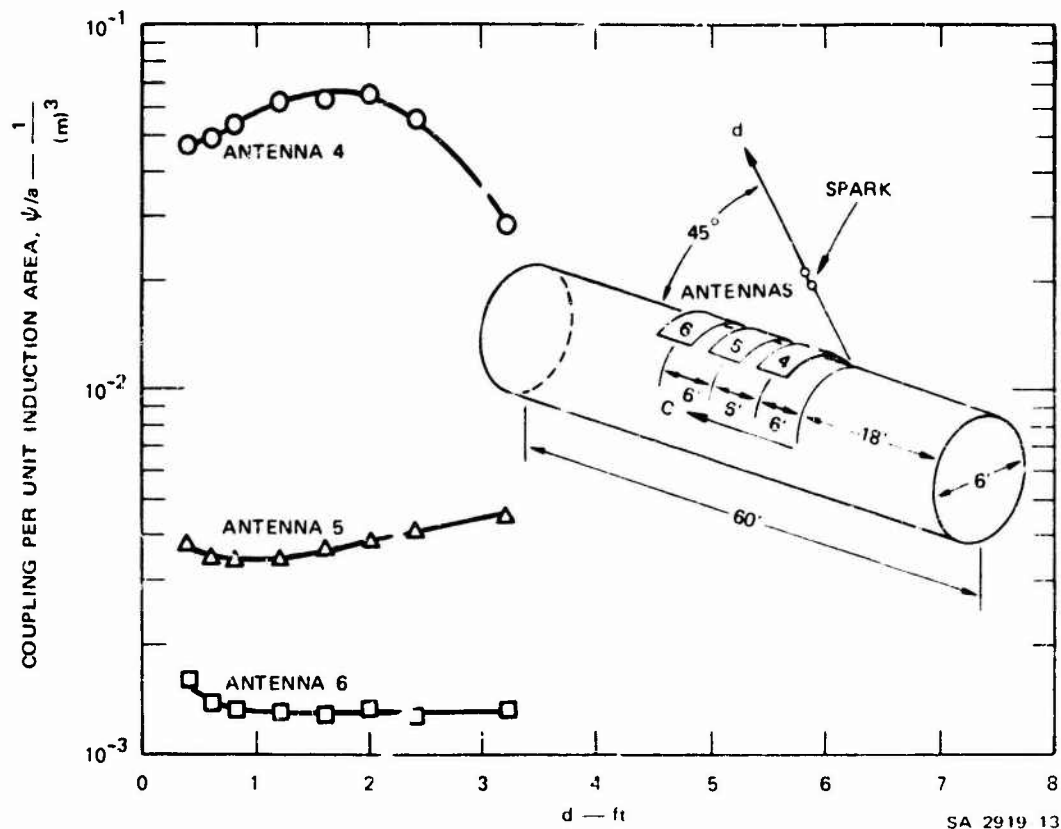


FIGURE 9 NOISE COUPLING TO CANOPY

dielectric window cut in the skin of an aircraft. The measured and calculated values of coupling for this antenna configuration are also shown in Figure 10. It should be noted that the coupling is presented as the coupling factor  $\psi$ , not normalized by the antenna induction area as was done earlier. Presenting coupling in terms of  $\psi$  is appropriate in this case since the current induced in the 12-gage wire by a streamer discharge will not be affected by the length of the wire. This is true because the region of the antenna wire in the immediate vicinity of the streamer is most important in coupling streamer signals. It should not be inferred from this that the streamer noise is independent of the length of the antenna and dielectric region. A longer region means a higher total charging current and consequently a higher prf (.) and a higher streamer noise level.

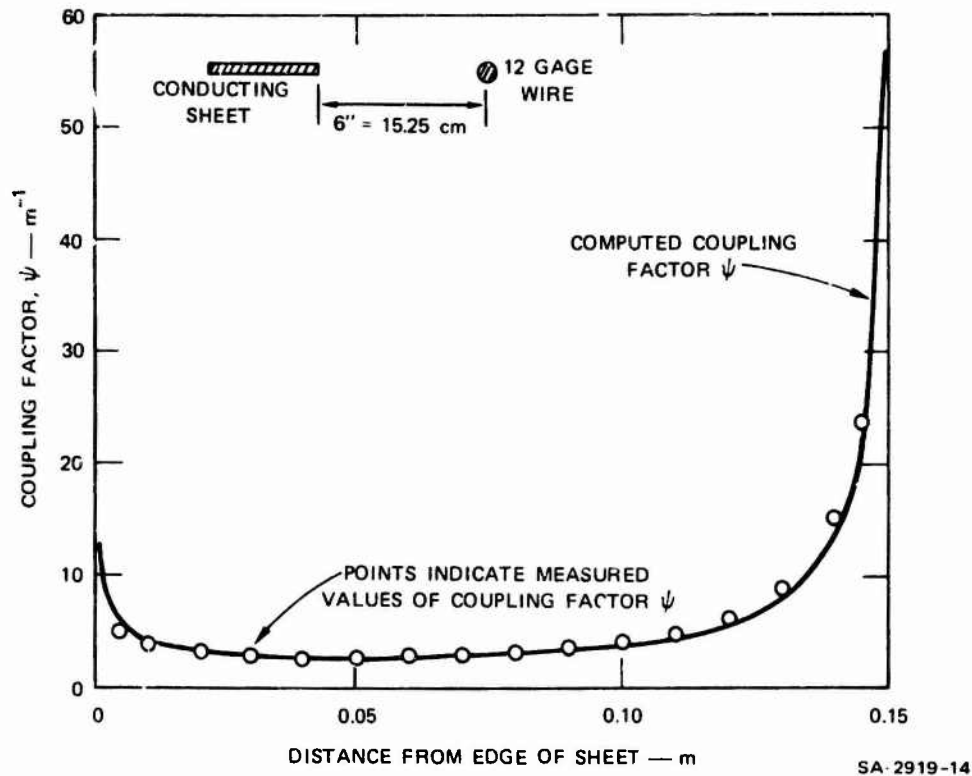


FIGURE 10 CALCULATED VALUES OF COUPLING FACTOR COMPARED TO VALUES MEASURED BY FIELD PROBE

Although a completely idealized geometrical arrangement such as that illustrated in Figure 10 is not likely to be found on a flight vehicle, the structure is sufficiently similar to the case of a slot cut in a vehicle's skin that the results are of interest. It is evident that the coupling is quite uniform, with a value of roughly  $3 m^{-1}$  over most of the gap, and that it increases only in the high-coupling-field regions in the vicinity of the wire and the edge of the sheet.

Also considered in Ref. 7 was the coupling geometry of one of the special radome antennas used in the B-47 flight tasks in that program and illustrated in Figure A-1(a). Here, because of the three-dimensional nature of the geometry, it was found that the coupling varies with position on the radome surface. It was found, however, that the magnitude of the coupling is of the same order as in the case of the idealized geometry of Figure 10. Indeed, the average streamer coupling for the radome of Figure A-1(a) is roughly  $\psi = 3 m^{-1}$ .

#### D. Equivalent Noise Field

Although the terminal noise current completely specifies the precipitation-static noise response of an antenna, terminal current is not a familiar term. Furthermore, since the terminal current induced in an antenna depends on the antenna characteristics, the terminal current is of no general value unless the antenna characteristics are also specified. Thus the precipitation-static noise data would be more convenient if they were expressed in terms of the field intensity required to generate the calculated terminal current in the antenna. Although the antenna noise current depends on size and sensitivity, the equivalent noise field applies to any antenna installed at the specified location. In particular, one generally knows the desired signal field-strength environment in which his system must function. If he also is able to express p-static noise in terms of equivalent-noise-field strength, he can immediately specify the ratio of signal to precipitation-static noise in his system.

Consider first the low-frequency case in which a dipole-type antenna mounted on the aircraft will have the radiation pattern of an elementary dipole.<sup>13</sup> The characteristics of the antenna are determined by specifying the direction of the dipole axis and the induction area,  $a$ , of the antenna, which is defined as

$$a = \frac{q}{\epsilon_0 E_1} \quad (10)$$

where  $E_1$  is the field intensity of the incident wave,  $q$  is the value of the induced charge on the antenna, and  $\epsilon_0 = (1/36\pi) \times 10^{-9}$  farad/meter. Bolljahn in Ref. 13 shows that  $h_e$  (effective height) and  $a$  for a given antenna are related through the expression  $\epsilon_0 a = h_e C$  where  $C$  is the capacitance of the antenna.

For the low-frequency case being considered, the current flowing at the short-circuited antenna is  $j\omega Q$ . Thus, using Eq. (10) we may write  $I_{sc} = j\omega\epsilon_0 a E_i$ . Rearranging and making an analogy between noise and signal, we obtain

$$|E_n| = \frac{|I_n|}{\omega\epsilon_0 a} \quad (11)$$

where  $I_n$  is the terminal noise current, and  $E_n$  is defined as the equivalent noise field.

As the frequency is raised above the quasi-static range, the antenna can no longer be represented by a simple dipole. In calculating  $|E_n|$ , therefore, it is necessary to account for changes in the radiation pattern and for the effects of aircraft resonances. In Ref. 4, equivalent noise fields at the KC-135 fin cap for frequencies of 2 MHz and higher were calculated using probe-antenna noise currents together with probe-antenna data. Since antenna gain varies with direction of signal arrival, the equivalent noise field calculated in Ref. 4 did not have a unique value for a given frequency, but was a function of direction. A comparison of the results of noise-field calculations using radiation patterns with results from quasi-static theory indicated that the error stemming from the use of the simpler quasi-static theory is not greater than that resulting from small changes in direction of propagation. Thus, it was concluded in Ref. 4 that the quasi-static method provides a simple method for estimating the order of magnitude of equivalent noise field at a given antenna location when pattern and impedance data for an antenna at that location are not available. Quasi-static estimates of antenna properties are used in this report in calculating noise fields.

## E. Aircraft Charging

### 1. Total Aircraft Charging Current (Corona)

To properly proceed with the planning of a discharger installation, it is necessary to estimate the charging that one should expect on the aircraft under investigation. Since extensive flight-test and laboratory studies of charging were made on the 707 prototype, it is convenient to structure the analysis so that these existing data can be interpolated and applied to the aircraft in question. Actually, the approach is to estimate the ratio of the new aircraft current to the 707 current when the two aircraft are operated in the same precipitation conditions. To provide a concrete illustration, the procedure will be carried out here for the case of the F-4 aircraft.

The precipitation charging current to a vehicle is given by

$$i = q_p c v A_{\text{eff}} \quad (12)$$

where

$q_p$  = Charge per particle

$c$  = Particle concentration in cloud

$v$  = Aircraft velocity

$A_{\text{eff}}$  = Effective intercepting area of aircraft.

Since we have assumed that the two aircraft are operating in the same precipitation, the first three terms on the right of Eq. (12) will be the same for the two aircraft when they are operated at the same speed. In this case, the ratio of the charging currents will be given simply by the ratio of the effective intercepting areas.

If the aircraft operate at different speeds, the situation is only slightly more complicated. Laboratory tests<sup>11</sup> confirmed by flight tests<sup>14</sup> indicate that the individual particle charge  $q_p$  varies only slightly with speed in the speed range of present day aircraft.  $A_{eif}$  will also vary somewhat with speed.

Let us now consider the question of determining the effective intercepting area of an aircraft of interest. Although considerable analytical work has been done to predict intercepting areas of aircraft flying in clouds composed of spherical water droplets, the ability to obtain these solutions is critically dependent on the fact that the drag coefficient of a moving sphere can be determined. These results cannot be applied directly to the case of an aircraft operating in a cloud composed of irregularly shaped ice crystals for which the drag coefficient cannot be determined. Thus, in estimating ice-crystal impingement on aircraft, it is necessary to rely heavily on flight-test experimental results and to use the results of water-droplet impingement calculations to indicate trends as various parameters such as size are varied. The procedure is not satisfying, in that considerable fitting and approximating must be done. (Until more analysis or flight testing is carried out, no other approach is possible.) For example, it is indicated on page 54 of Ref. 4 that the effective area of the 707 is a small fraction of the projected area (roughly 20% to 25% interception efficiency). On page 119 of the same report, it is observed that the percent of the frontal area of an ellipsoid effective in intercepting particles varies inversely with the length of the body.<sup>15-17</sup> From this it was concluded in Ref. 4 that in the case of similar aircraft, the ratio of the effective areas  $A$  is given by the ratio of the spans of the aircraft  $S$ :

$$\frac{A_{F-4}}{A_{707}} = \frac{S_{F-4}}{S_{707}} \quad (13)$$

Later the problem of scaling was reviewed, and it was noted that the frontal area of the airfoils was generally almost equal to the frontal area of the fuselage. It was argued, then, that since the percent effectiveness of the airfoils is much higher than the effectiveness of the fuselage, the charging would stem primarily from the airfoils. Thus, the way in which aircraft charging is affected by changes in size is determined by the way in which airfoil interception area varies with size. Considerably after the publication of Ref. 4 the authors discovered NACA RM No. 9A05,<sup>18</sup> in which a study of the impingement of water droplets on several airfoils was reported. The data in this NACA report (reproduced in Figure 16) indicate that, in the vicinity of 20% to 25% interception efficiency, percent intercepting area varies inversely with airfoil scale. As indicated earlier, flight-test data obtained on the Boeing 367-80 aircraft (the prototype of the 707 and KC-135) indicated that during much of the time the intercepting area was 50 ft<sup>2</sup> (25% of the airfoil frontal area) or less as shown in Table III of Ref. 4. These last observations confirm that the relationship of Eq. (13) is correct for estimating the effects of scaling on aircraft charging current. Careful inspection of Figure 11 indicates that the percent intercepting area varies inversely with aircraft scale up to roughly a 25% interception efficiency, and that, for small aircraft, the percent interception grows more slowly with decreasing size. Thus for the F-4 operating at KC-135 speeds, the charging current would be somewhat lower than predicted by Eq. (13). However, since the F-4 can operate at supersonic speeds, the appropriate free-stream Reynold's number for the F-4 case in Figure 11 will be higher than for the KC-135 (twice as high

SOURCE: Ref. 19

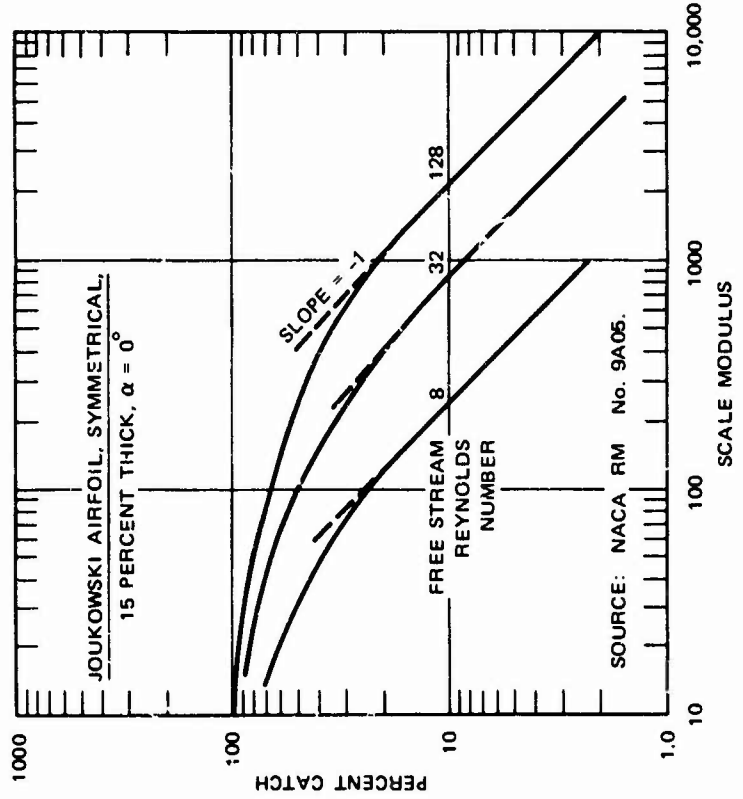
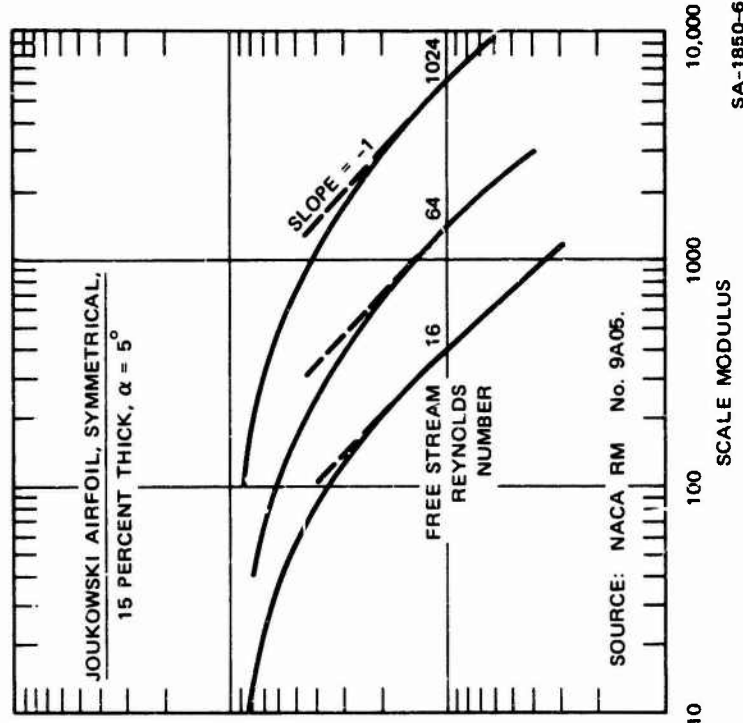


FIGURE 11 PERCENT INTERCEPT AS A FUNCTION OF AIRFOIL SIZE. Source: Ref. 18.

for  $M = 2$ ). This has the effect of continuing the straight-line portion of the curves in Figure 11 to a scale modulus appropriate for the F-4. Accordingly, it is appropriate to use Eq. (13) in estimating F-4 charging current from KC-135 flight-test data.

The wing-spans of the F-4 and KC-135 are as follows:

$$S_{F-4} = 39.3 \text{ ft}$$

$$S_{707} = 130 \text{ ft}$$

Using these values in Eq. (13) we obtain

$$I_{F-4} = 0.3 I_{707} \quad (14)$$

Values of total charging current calculated in this manner are required in the estimation of corona-noise levels to be expected on an airframe and in devising discharge installations.

## 2. Localized Charging (Streamers)

To determine the noise levels generated by streamer discharges, it is necessary to be able to specify the charging current responsible for generating the streaming. Attempting to make precise calculations of dielectric charging current is even more difficult than calculating total charging current. Accordingly, we will adopt the procedure of using empirical estimates based on flight-test measurements made on the F-4 tests described in Ref. 14. The test aircraft included provisions for measuring the current arriving on the windshield and on isolated patches on the radome.

In formulating the computer model, for the windshield and canopy we will use:

$$I_{\text{diel.}} = \frac{1}{2} \frac{A_{\text{front. diel.}}}{A_{\text{front. aircraft}}} I_{\text{T aircraft}} \quad (15)$$

where  $I_{\text{diel.}}$  is the current arriving on the windshields or canopy,  
 $A_{\text{front. diel.}}$  is the frontal area of the dielectric region in question,  
 $A_{\text{front. aircraft}}$  is the projected frontal area of the aircraft, and  
 $I_{\text{T aircraft}}$  is the total charging current to the aircraft.

For the radome we will use:

$$I_{\text{radome}} = \frac{A_{\text{forward 3 ft}}}{A_{\text{front. aircraft}}} I_{\text{T aircraft}} \quad (16)$$

where  $I_{\text{radome}}$  is the current arriving on the radome and  $A_{\text{forward 3 ft}}$   
is the projected frontal area of the forward three feet of the radome.

### III COMPUTER MODELING OF EXISTING DATA

#### A. General

The experimental and analytical data regarding p-static noise discussed in Section II were processed appropriately, and made part of the computer program. In some cases, this meant using an analytical expression or approximation to the desired parameter. In other cases where the data did not lend itself to approximation, it was simply stored in tabular form.

A brief description will be given here of the approach taken in order that the reader be familiar with the contents of the program and how it was derived.

#### B. Corona Noise

The total charging current arriving on the aircraft is calculated using Eqs. (12) and (13), where  $q_p$  and  $c$  have been replaced by an expression relating these quantities to aircraft speed and cloud type (e.g., cirrus, stratacumulus, frontal snow). The free parameters in this expression have been adjusted such that the charging current to a 707 flying in the same frontal snow conditions,  $I_{707}$ , is 4 mA. This adjustment was made to correspond to the highest charging conditions encountered on the 707 prototype during the flight-test program of Ref. 4. The statistical data presented in Figure 27 of Ref. 4 indicate that this charging is exceeded only 0.002% of the flight time on a jet transport. Thus, the noise levels obtained from the computer program (which are related to the charging current) will be typical of the most severe charging conditions for a given altitude, speed, and type of precipitation

particle. The program also includes a printout of the probability that the actual charging current will exceed the calculated charging current.

Provisions are included in the program to allocate the discharge currents among the various aircraft extremities. Based on the work of Ref. 4 the currents are apportioned approximately as follows:

$$\begin{array}{ll} \text{Each empennage tip} & 1/7 I_T \\ \text{Each wing-tip} & 2/7 I_T \end{array}$$

Specifying the discharge regions in the computer code was necessary since the coupling to the noise source depends critically on the aircraft extremity from which the corona discharge is occurring.

Provision is also made for quieting selected discharge locations. This quieting, essentially a 40-dB noise reduction, allows the electromagnetic compatibility (EMC) engineer the opportunity to study the effect of installing corona quenching or quieting devices (p-static discharges for example) at selected locations.

Once the corona current discharged from an extremity is determined, Eqs. (2) through (6) are used to calculate the source spectrum of the RF noise that this discharge generates. The received noise spectrum resulting from the discharge at the extremity in question is calculated by convolving the noise-source spectrum with the appropriate coupling function from Figure 6 for the antenna location and extremity under consideration. The total received noise spectrum is obtained by summing the contributions from each of the extremities on an rms basis.

Since the coupling data of Figure 6 are experimental and do not lend themselves to an easy analytical description, they are read into the program from data cards and stored in the program in tabular form. This technique, while somewhat cumbersome, has the advantage that when additional coupling data become available, they can be used and no program modifications are necessary.

The program includes provisions to scale the frequencies of the resonances in the coupling curves of Figure 6 to make them appropriate for the aircraft under investigation. Eq. (9) is used to adjust the magnitude of the coupling function according to the size of the aircraft.

Once the total received noise spectrum is calculated, Eq. (11) is used to express the received noise signal in terms of an equivalent noise field at the antenna location. It should be observed at this time that corona-noise-coupling data are available only for an aircraft the shape of a KC-135. However, the same data have been applied to aircraft such as the F-4,<sup>14</sup> which is quite dissimilar from the KC-135, with remarkably good results. Thus, until additional coupling data are generated, there is no choice but to use existing data. As described above, provisions are included in the program to incorporate new coupling information as it becomes available.

### C. Streamer Noise

The current arriving on the dielectric surface under consideration is calculated using Eq. (15) for the case of a structure such as a windshield or canopy, and using Eq. (16) for a radome. To use these equations, it is necessary to know the total aircraft charging current  $I_T$ . This is available from the earlier corona-noise calculations.

Noise-source calculations are made using Eq. (A-3) of Appendix A. In the first term of this equation,  $I_m$  and  $v$  are simply constants related to the characteristics of a streamer discharge, and the PRF is found from the dielectric charging current by

$$v = \frac{I_{\text{diel.}}}{1.5 \times 10^{-9}} \quad (17)$$

The second term of Eq. (A-3) is given by Eq. (A-5), in which all the terms except  $\omega$  are constants related to the characteristics of the streamer discharge. The last term in Eq. (A-3) is given in Table A-1 for three different geometric arrangements. Since it was shown that the noise-spectrum characteristics are not sensitive to the shape of the dielectric region, the computer program uses the third expression in Table A-1. In this case the term  $W$  is the length in meters of the minimum characteristic dimension of the dielectric region under consideration--i.e., the width of a rectangular region. (The term  $W$  may be thought of as roughly twice the length of the longest possible streamer discharge on the region in question.)

It should be noted that the last expression in Table A-1 includes the coupling factor  $\psi$ , which must be specified. Three different physical arrangements of "antenna" and streamer source can be specified. The first is that illustrated in Figure 8, where the antenna is located on the fuselage aft of the region (such as the radome) in which the streamering is occurring. The data of Figure 8 have been stored in the program, so that it is necessary only to specify the diameter  $F$  of the fuselage at the antenna location and the distance  $d$  the noise source is located ahead of the metallic portion of the fuselage.

The second streamer configuration is illustrated in Figure 9, where the antenna is located on the fuselage beneath a windshield or canopy on which streamers are occurring. It is evident from Figure 9 that the coupling is relatively independent of the location  $d$  of the discharge on the canopy. Accordingly, the data stored in the program use the approximation that the coupling is entirely independent of  $d$ . It is necessary only to specify the distance  $C$  of the antenna aft of the front edge of the canopy.

It should be noted that in both Figure 8 and Figure 9, the noise source is sufficiently far removed from the antenna that the noise

coupling will be affected by antenna induction area  $a$ . Thus the noise coupling is presented in normalized form  $(\Psi/a)$  and it is possible to use Eq. (11) directly to calculate at equivalent noise field  $E_n$ .

The third streamer coupling configuration considered is illustrated in Figure 10. Here a wire is located on the underside of the dielectric on which streamers are occurring. With this arrangement the streamer noise source is so close to the wire "antenna" that the noise picked up by the region of the wire in the immediate vicinity of the streamer dominates. Thus the streamer coupling is independent of wire length (i.e., independent of "antenna" induction area  $a$ ). In this case the computer output indicates the short-circuit current induced in the wire rather than the equivalent noise field at the wire location.

#### D. Verification of Computer Model

##### 1. General

To test the functioning and accuracy of the computer modeling, calculations were carried out to predict precipitation-static noise levels under various conditions. Vehicle types and sizes were chosen to correspond as closely as possible to the vehicles employed in the flight tests described in Refs. 4 through 7, and 14. Precipitation charging conditions also were chosen to duplicate as nearly as possible the conditions encountered during the flight tests. During the flight tests, measurements were made of both streamer and corona noise, and three different types of aircraft were used. Thus, it is possible to verify the computer model under a gratifyingly large variety of conditions.

## 2. Corona Noise

### a. 707 Belly Antenna

In the flight tests of Refs. 4 and 5, the 707 prototype aircraft was operated without any p-static noise-reduction provisions in light cirrus clouds such that the total charging current to the aircraft was 250  $\mu$ A. Measurements were made of noise current induced in the belly antenna. These measured data have been interpreted as equivalent noise field, and are plotted as the five data points in Figure 12.

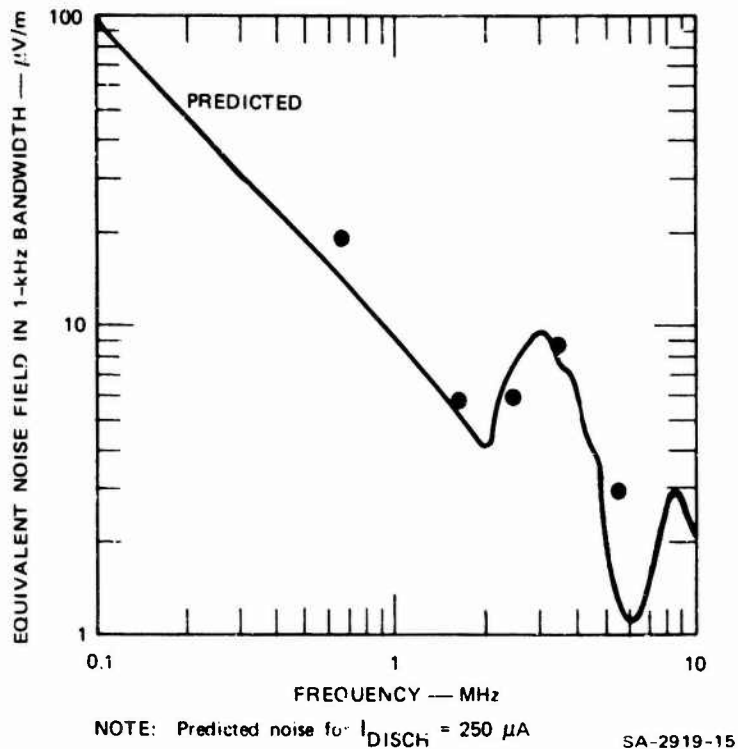


FIGURE 12 CORONA-NOISE FIELDS AT 707 BELLY ANTENNA

Also plotted in Figure 12 is the curve of equivalent noise field at the 707 belly antenna location predicted by the computer model. In the computing of the predicted noise field, the program was artificially constrained to a charging current of 250  $\mu$ A typical of the very light cirrus clouds encountered during this portion of the

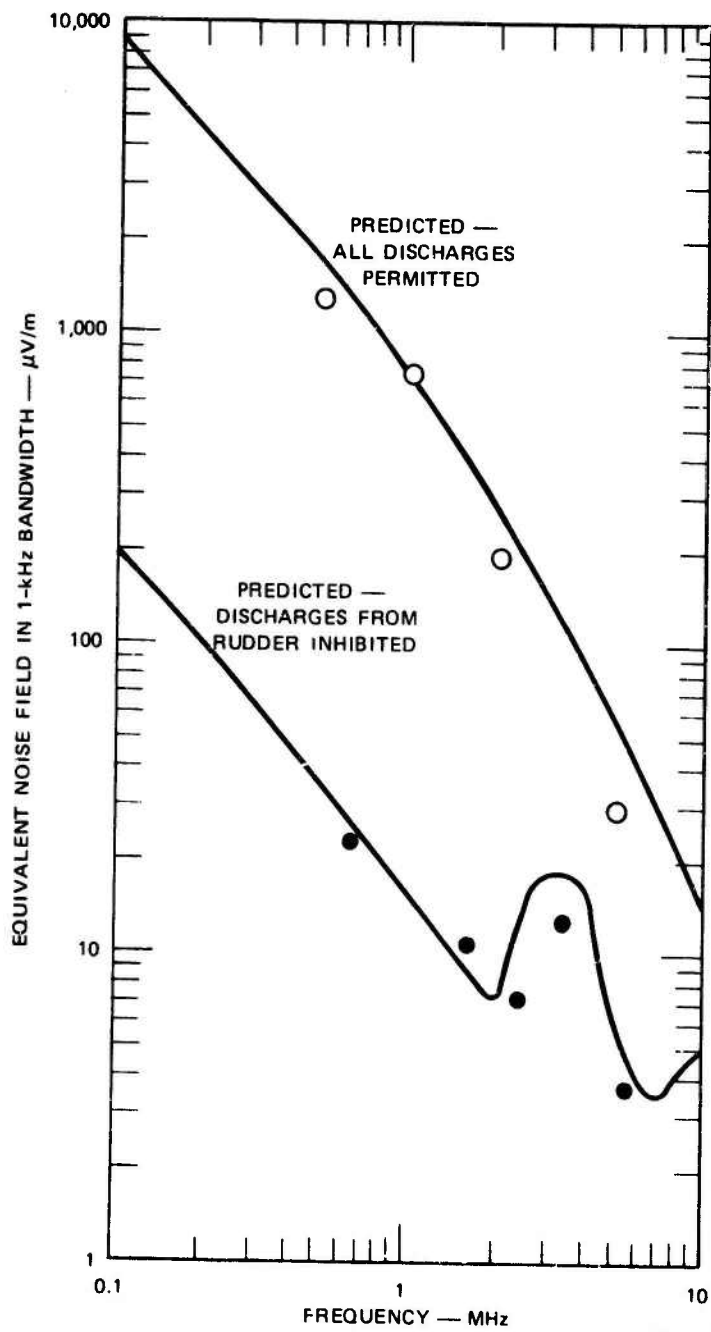
flight-test program. (The computer model would normally estimate a charging current of 1 mA to a 707 aircraft in cirrus.)

It is evident from Figure 12 that the computer model is remarkably accurate in predicting all the details of the corona noise induced in the belly antenna. The absolute level of the noise-field intensity is accurately predicted, and the airframe resonances are correctly represented.

b. 707 Tail-Cap Antenna

In the 707 flight-test program of Refs. 4 and 5, noise measurements were also made on the tail-cap antenna when the aircraft was operated in light cirrus such that the total aircraft charging current was 250  $\mu$ A. In the first flight tests, the aircraft was entirely unmodified so that corona discharges could occur from each of the airfoil extremities. The noise-field intensities measured in these flights are shown as circles in Figure 13. Also shown in the upper part of the figure are the noise fields at the tail cap predicted by the computer model. (As before, the computer program was constrained to a charging current of 250  $\mu$ A typical of the extremely light cirrus clouds encountered during this test series.) It is evident from the upper part of Figure 13 that the computer code accurately predicted the magnitude and spectral character of the noise in the tail-cap antenna when all corona discharges were permitted.

Later in the same series of flight tests, electrical insulating tape was applied to the trailing edge of the rudder of the 707 test aircraft. In this way corona discharges from the rudder were inhibited. The noise fields measured at the tail-cap antenna under these conditions are shown as the dots in Figure 13. Shown for comparison in the lower part of the figure is a curve giving the noise spectrum predicted by the computer model for tail-cap antenna noise



SA-2919-16

FIGURE 13 CORONA-NOISE FIELDS AT 707 TAIL-CAP ANTENNA

when discharges from the rudder are inhibited. Again it is evident that the computer code accurately predicted both the magnitude and the character of the noise spectrum.

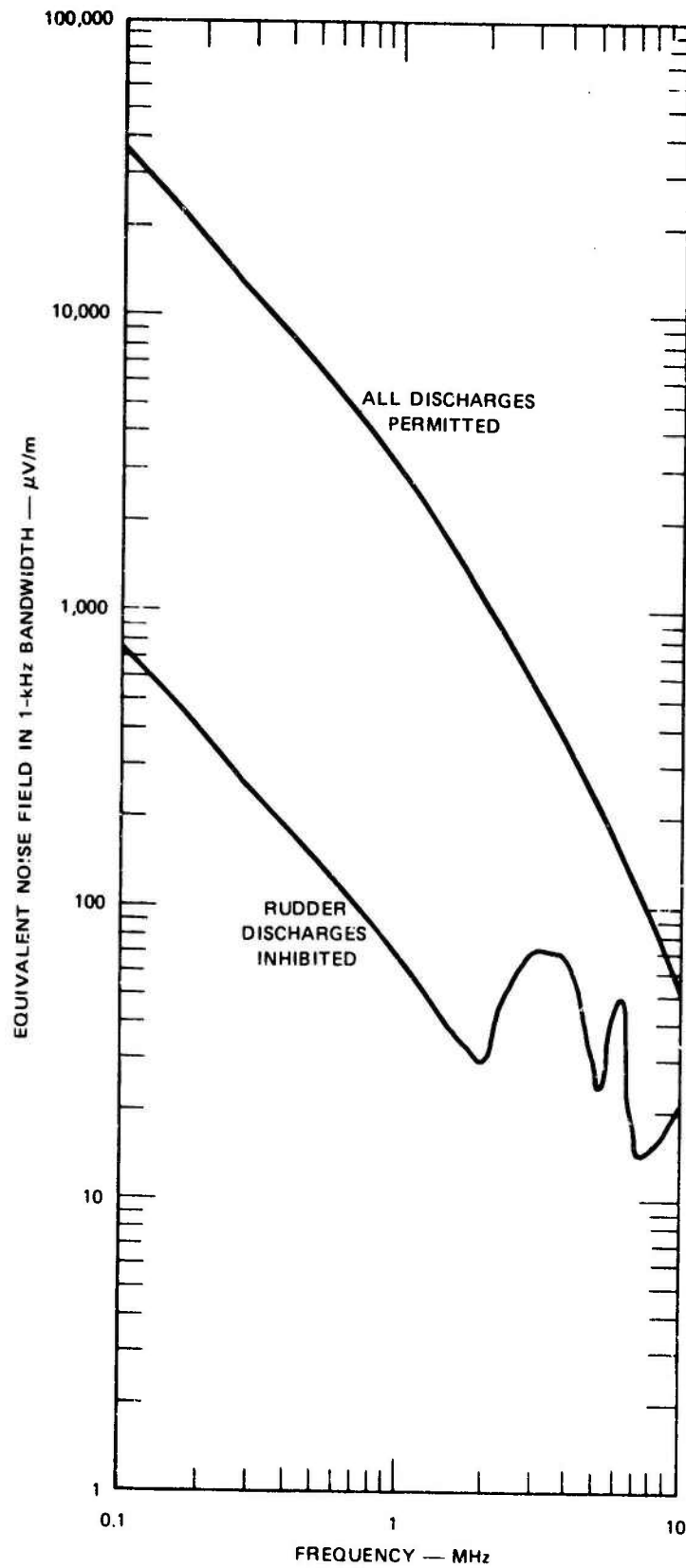
The utility of being able to request that the computer model suppress one of the noise sources is evident in Figure 13. Here it is evident that noise generated by discharges from the rudder dominates the tail-cap antenna noise environment. By eliminating the rudder corona, the noise level is reduced by almost 40 dB at the lower frequencies. Such information is highly significant to the EMC engineer since it means that in developing noise-reduction techniques, great care must be exercised to make certain that rudder corona noise is eliminated.

In comparing the data of Figure 12 with the lower curve in Figure 13 we see that the noise levels are comparable, and that the effects of airframe resonances are evident in the peaks of noise levels at frequencies of roughly 3 MHz in both sets of data. It should also be observed that, in these two cases, the noise levels are substantial, and that functioning of radio systems could be improved by further noise reductions.

To further demonstrate the utility of the computer model, a calculation of tail-cap antenna noise was carried out for the case of the 707 aircraft operating in frontal snow where the aircraft charging current is 4 mA. The resulting noise levels shown in Figure 14 are extremely severe--even with rudder discharges inhibited.

c. F-4 Tail-Cap Antenna

A further test of the computer model was its ability to predict noise levels on an aircraft much smaller than the 707. Accordingly, the computer code was used to predict the noise levels to be expected at the tail cap of an F-4 aircraft operating in cirrus clouds.



SA-2919-17

FIGURE 14 PREDICTED CORONA-DISCHARGE NOISE FIELDS ON 707 TAIL-CAP ANTENNA IN FRONTAL SNOW

It was recognized that the shape of an F-4 is greatly different from that of a 707, and that coupling data gathered using a model of the 707 was not appropriate for the F-4, so that good agreement between measured and predicted data should not be expected. The computer results are shown in Figure 15 along with data measured in the F-4 flight-test program of Ref. 14.

It is noteworthy in Figure 15 that eliminating corona discharges from the rudder affords considerably less noise reduction than it did on the 707 (see Figure 13). This stems from the fact that the F-4 is sufficiently small that coupling from the fin-cap to the wing and elevator tips is almost as high as the coupling from the tail-cap to the rudder. Thus rudder corona noise is not as dominant a source of interference on the F-4.

It is also evident that the degree of agreement between predicted and measured noise in Figure 15 is not as good as it was for the 707. This is reasonable since the coupling data used in the present computer model are not strictly appropriate for the F-4. Instead of concentrating on the differences between the predicted and measured results in Figure 15 it is more important to observe that the predicted data are still in remarkably good agreement with the measurements. In fact the difference between predicted and measured results is of the same order as the difference caused by flying the aircraft in a different cloud type--e.g., stratocumulus instead of cirrus.

In general, we should conclude that the computer model does a remarkably good job of predicting the noise levels on an aircraft differing considerably from the 707 in both shape and size.

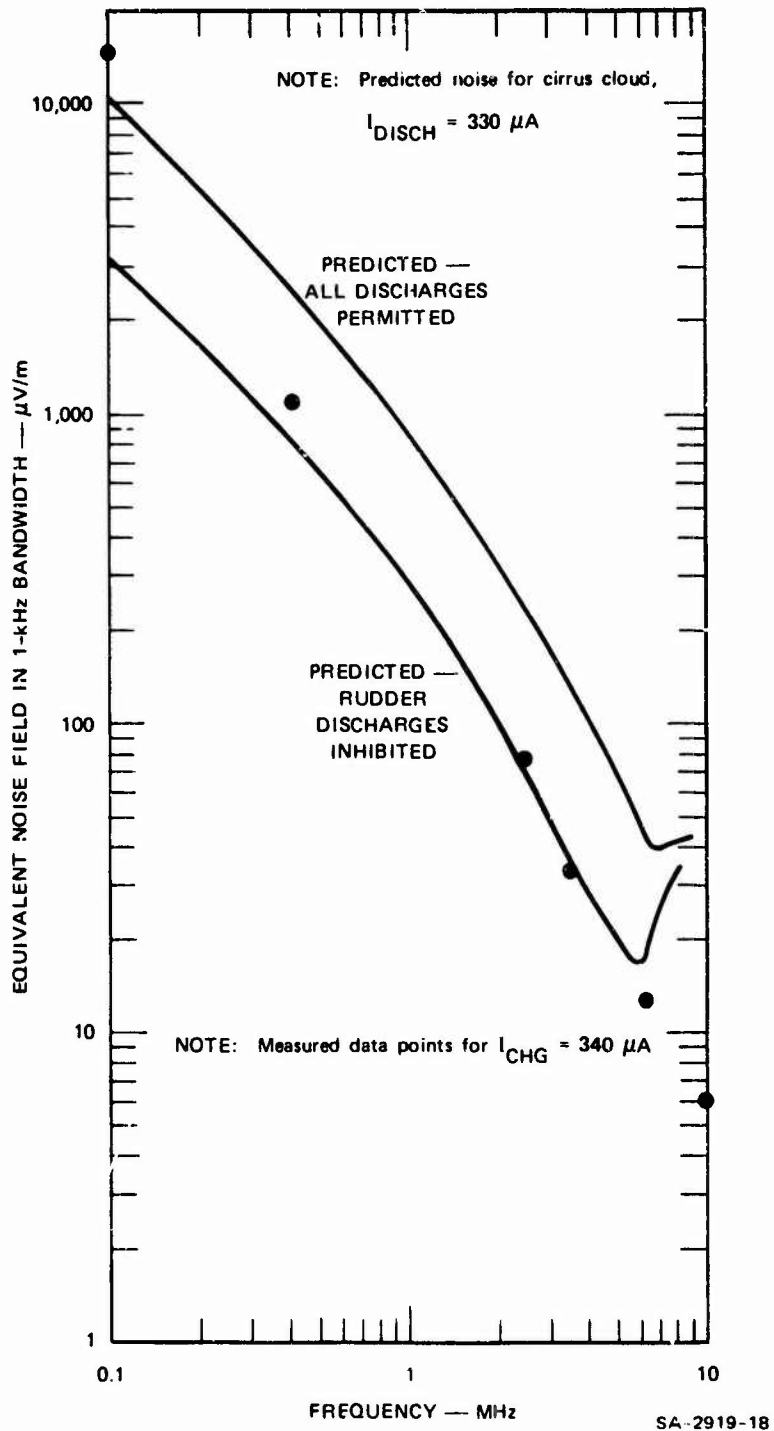


FIGURE 15 CORONA-NOISE FIELDS AT F-4 TAIL-CAP ANTENNA

d. F-4 Belly Antenna

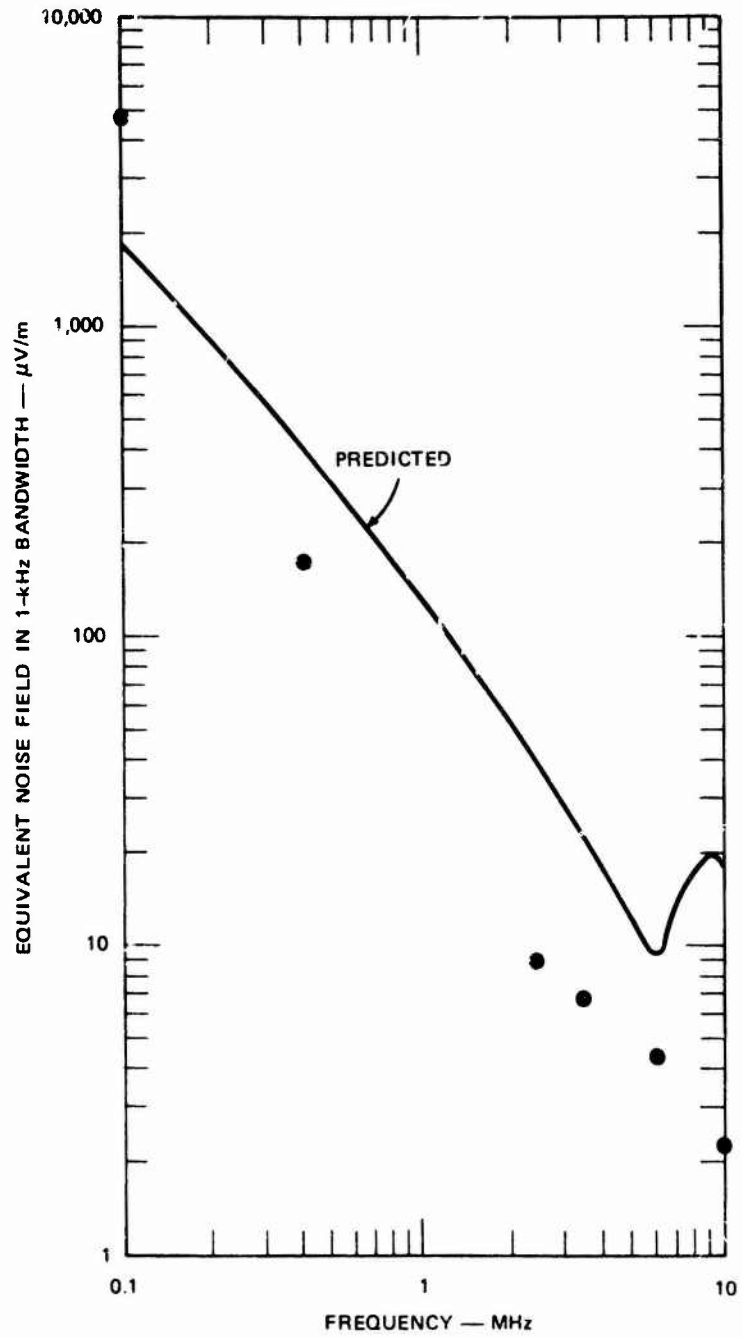
As an additional test of the general applicability of the computer model, it was used to predict the noise level on the belly of the F-4 aircraft. The results of this calculation are shown in Figure 16. It can be argued that, because of the general symmetry of the aircraft's structure, the belly data should also be applicable to the case of an antenna mounted on the top of the fuselage. Accordingly, data measured using a Chelton "towel-bar" antenna mounted on the top of the fuselage of the F-4 of Ref. 14 are shown in Figure 16 for comparison. Again, it is evident that the computer output provides an acceptable estimate of the noise actually measured in flight.

Thus, we should conclude from Figure 16 that the computer model can be stretched considerably and applied to situations other than those precise ones for which there are measured coupling data.

3. Streamer Noise

a. B-47 Coated Radome Antenna

The streamer-noise portion of the computer model was checked by comparing its predictions with flight-test data generated on the B-47 aircraft used in the tests of Refs. 6 and 7. The B-47 was equipped with a special nose section divided into separate metal cavities with an acrylic radome section forming the outside wall of each of the cavities. Two of these cavities, located on opposite sides of the fuselage, were each fitted with a short antenna wire which measured the noise at its location. The acrylic cover over the first of these cavity sections was coated with electrically conducting paint to prevent streamering on its surface. The second cavity cover was left uncoated so that electric charge could accumulate on the acrylic surface, thereby causing streamer discharges to occur on the uncoated radome section.



SA-2919-19

FIGURE 16 CORONA-NOISE FIELDS AT F-4 CHELTON ANTENNA (top of fuselage)

The streamer noise generated on the uncoated section coupled into its antenna and also into the antenna under the coated section on the opposite side of the aircraft.

The coupled streamer noise current measured at the coated radome section is shown in Figure 17.

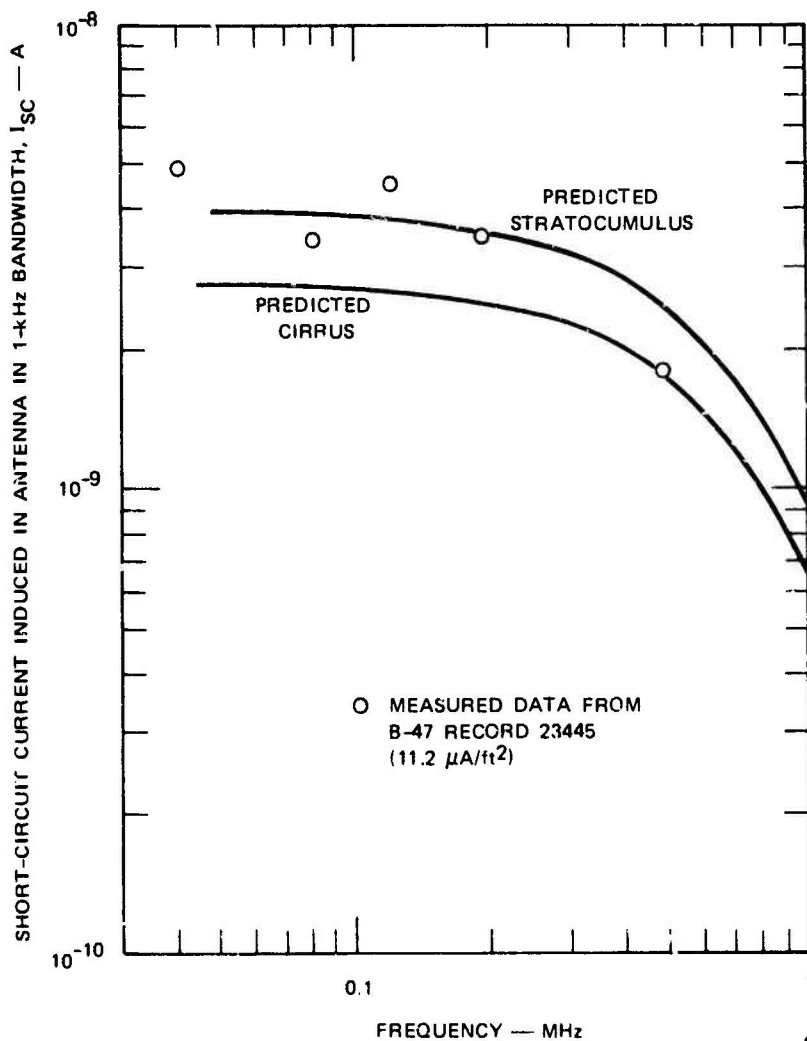


FIGURE 17 NOISE SPECTRUM IN COATED RADOME SECTION ON B-47 AIRCRAFT

Also shown in the figure are predicted noise currents generated by the p-static computer model for the case of an antenna mounted on an aircraft such that  $F = 1$  ft and  $d = 2$  inches for the case of cirrus and stratocumulus clouds. It is evident that the predicted noise currents are in good agreement with the measured data.

b. B-47 Uncoated Radome Antenna

Noise measurements were also made on the antenna under the uncoated radome section. This arrangement corresponds to the case of an antenna such as those often mounted on the inside surface of a pilot's canopy. Here the antenna wire is positioned on the back surface of the frontal dielectric on which streamers are occurring. Obviously the coupling in this condition is high, so that the induced noise currents should be high.

Noise currents measured in the antenna behind the uncoated radome surface are shown in Figure 18. Unfortunately, as is indicated in Ref. 7, following the flight tests it was found that the preamplifier used with this antenna could be overdriven by the individual streamer noise pulses so that the measured noise spectrum is not truly representative of that existing at the antenna. In particular the low-frequency content of the measured noise was demonstrated to be accentuated. In spite of this shortcoming in the measured data, it is interesting to note that the measured noise currents in the uncoated antenna are several orders of magnitude higher than those measured under the coated radome.

Also plotted in Figure 18 are the short-circuit noise currents predicted by the computer model for the uncoated radome antenna. The general noise levels are in good agreement with the measured data. The disparity in the shapes of the measured and

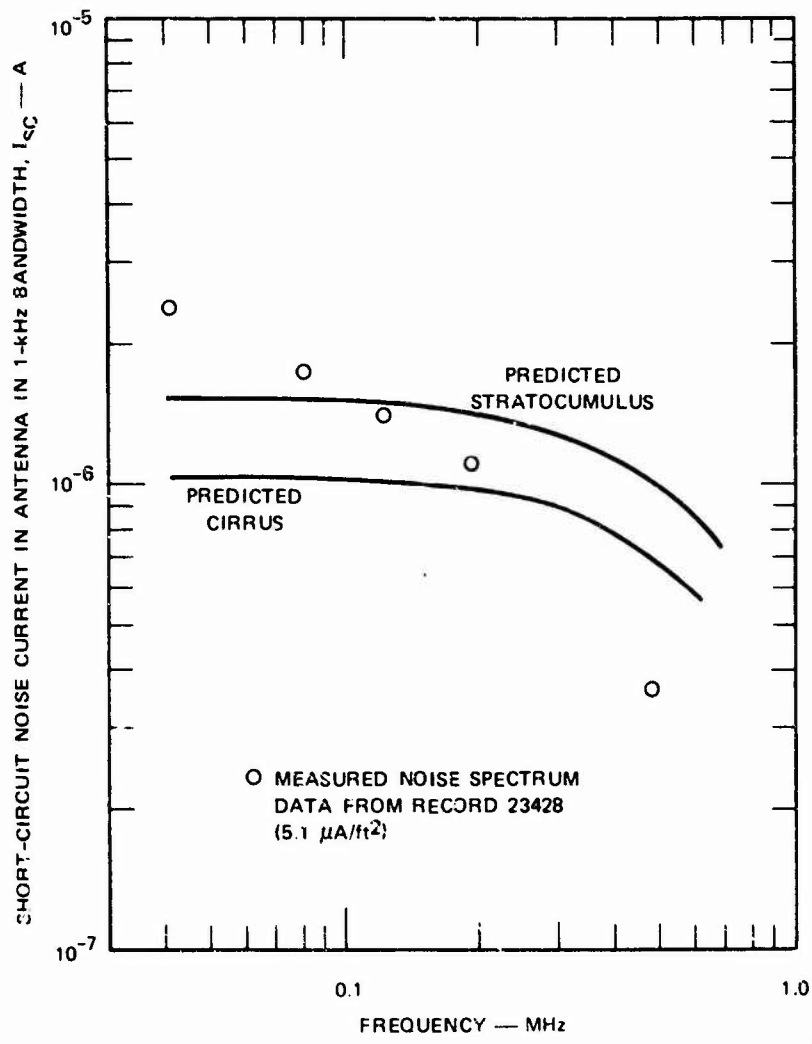


FIGURE 18 NOISE SPECTRUM IN UNCOATED RADOME ANTENNA SECTION ON B-47 AIRCRAFT

computed spectra should undoubtedly be attributed to the shortcomings of the B-47 flight-test instrumentation.

It should be concluded, therefore, that the computer model is able to predict streamer noise spectra with good accuracy, and that the predicted results can be applied with confidence.

## IV APPLICATION AND LIMITATIONS OF COMPUTER MODEL

### A. General

Since the computer model developed here is entirely based on the results of earlier work, its applications and limitations are circumscribed by this earlier work. In each of the previous programs, an effort was made to ensure that the results were as generally applicable as possible. However, practical considerations dictated that the flight tests and supporting laboratory work restrict themselves to the consideration of a limited number of aircraft. As a result the existing noise-source data are of general applicability, since they are independent of vehicle design. Corona coupling, on the other hand, has been measured only for the KC-135 aircraft (which was used as the flight-test vehicle). The KC-135 corona coupling data can be scaled with no loss of accuracy to similar aircraft of different size, and can be applied with reduced accuracy to aircraft of other shapes. For corona noise, supporting flight-test data are available for the KC-135 and for the F-4 aircraft.

The streamer-noise data, while also somewhat limited, are of quite general applicability since they do not depend on aircraft design and RF resonance to the extent that the corona noise coupling does.

### B. Applications

#### 1. Corona Noise

Although corona-noise coupling measurements were made only for the case of a fin-cap located near the rear of the vertical tail and

for an ADF sense antenna on the belly of the KC-135, the results can be applied somewhat more generally. For example, the fin-cap coupling data can be applied with good accuracy to an antenna located anywhere on the top of the vertical fin. These might range from a probe antenna such as is used on the 707 to an electrically isolated portion of the fin structure such as that used on the DC-8.

The belly-antenna coupling data were measured for the case of an antenna located at the wing root as indicated in Figure 5. In view of the symmetry of the aircraft, however, these data also can be applied with little loss of accuracy to the case of an antenna located at the same fuselage station on the top of the fuselage. If necessary, the same coupling data can be used with reasonable accuracy to investigate coupling to antennas located as much as one-quarter fuselage length fore or aft of the wing-root position.

Although no coupling measurements were made for the case of an antenna located on a wing-tip, it is possible to do a reasonable job of predicting noise levels on these too. Looking at Figure 6 we note that for the tail-cap antenna, the highest noise coupling is to discharges occurring from the rudder. We may argue with reasonable validity that in the case of a wing-tip antenna the dominant source of corona noise will be corona discharges from the wing-tip trailing edge. Since a wing-tip is indistinguishable electrically from a fin-tip, the coupling from wing-tip antenna to wing-tips should be given quite accurately by the rudder-tip-to-tail-cap coupling curve of Figure 6.

A similar sort of argument is possible for the case of noise coupled into a wing-tip antenna from discharges on the rudder. Here we can invoke reciprocity and argue that the coupling is given by the wing-tip-to-tail-cap coupling of Figure 6.

In the case of noise generated on the opposite wing-tip and on the elevator tips, unfortunately, we cannot make use of the existing coupling data to determine coupling factors.

Since only the coupling data of Figure 6 exist at present, they must be applied to all aircraft regardless of shape or size. In the case of extremes such as a delta-wing fighter, for example, it would seem that the validity of using the KC-135 coupling data is doubtful. It must be recalled, however, that these data were reasonably accurate in predicting the corona noise levels on an F-4 aircraft in Ref. 14.

In using the program to study corona noise, it should be recalled that one of the outputs is the equivalent noise field at the "antenna" location. This information can be used directly as an input to the Introsystem EMC Analysis Program to analyze the noise coupled into the "antenna" (a wire, an aperture, or even a real intentional antenna) at the location in question.

In the case of situations involving radio receiving systems, the equivalent noise field at the antenna location is often the only parameter of interest. One can immediately determine whether the resulting signal-to-noise ratio is acceptable. If the p-static noise is unacceptably high, a knowledge of the noise-field intensity indicates to the EMC engineer the degree of corona noise reduction required by his system.

## 2. Streamer Noise

On most aircraft of standard design, the fraction of the frontal surface fabricated of highly insulating dielectric material has been small. This does not mean that the frontal surfaces have always been fabricated of metal. It simply means that where dielectric materials were used, it was almost always possible to coat the dielectric with a conductive layer such as a metal film or a conductive paint. Thus

the total current involved in streamer discharges has been much smaller than the corona current, and consequently the streamer-noise-source intensity is generally proportionally lower than the corona-noise-source intensity. Accordingly, it has been possible to restrict consideration of streamer noise to sources in the close vicinity of the receiving "antenna". For this reason available streamer coupling data have been generated exclusively for the case of antennas located near the dielectric surface on which the streamer discharges are occurring. Fortunately, constraints on aircraft design are such that these data are adequate to cover most cases of practical interest.

The main frontal regions of dielectric on an aircraft are the radome, the windshield, and the canopy structure. The PSTAT program is designed to treat the coupling of noise from streamers on these surfaces to "antennas" located on the fuselage of the aircraft. The output of the program is designed to provide either the equivalent noise field at the location of interest or the short-circuit noise current induced in the structure of interest. (To obtain the short-circuit current it is necessary to specify the "antenna" induction area.) These outputs permit the investigation of streamer effects on intentional antennas of receiving systems as well as noise coupling into inadvertent antennas formed by wires, cables, etc.

In some cases the "antenna" wire is located immediately below the surface on which streamers are occurring. Provisions are included in the PSTAT program to treat these areas. With this geometry, the signal induced in the wire is determined primarily by coupling to the region in the immediate vicinity of the streamer. Therefore the noise pulses are largely independent of antenna length so that a calculation of equivalent noise field is not appropriate. Consequently, the output of the program provides the short-circuit noise current induced in a wire on the back side of a dielectric. The wire, of course, may be an antenna wire, or cabling associated with an aircraft avionic system.

## C. Limitations

### 1. Corona Noise

Since the computer program was based on an existing technological base, it can be no better than the available base. Accordingly, there are restrictions on the regions of the aircraft for which noise-level calculations can be made. For the same reason, the coupling data are most accurate for aircraft shaped like the KC-135. No coupling data exist for vehicles such as rockets.

Since the coupling data were measured with a system that did not provide phase information, only the magnitude of the coupling factor is included in the program. For this reason, the program provides only noise-power spectral-density information. It is not possible at present to calculate amplitudes of individual noise pulses. (Such noise-pulse information is important in treating digital systems.) To calculate individual noise pulses it is necessary to have information on both the phase and magnitude of the coupling function.

Coupling information were generated only to frequencies of 12 MHz in the KC-135 measurement program. This sets the upper limit on the frequency range that may be considered.

All of the corona-noise spectral data depend on pulse shape and spectral measurements made on the program of Ref. 4. These measurements were carried out with state-of-the-art instrumentation available at that time. More recently, preliminary investigations using more modern spectrum-analyzer techniques appear to indicate that the spectrum does not decay as rapidly in the VHF region as was indicated by the work of Ref. 4. Over the region where corona noise is most severe, the noise-source data appear to be accurate.

## 2. Streamer Noise

As in the case of corona noise, the computer model was founded on the existing technological base. The geometries for which coupling data exist allow consideration of a reasonably wide variety of problems. It is likely, however, that situations may arise for which coupling data do not exist. Fortunately, the problem here is not as complex as in the case of corona-noise coupling, since the streamer source must generally be close to the affected "antenna" so that vehicle resonances are not important in determining the coupling.

The streamer noise-source data are based on oscillographic measurements of waveforms made during the programs of Refs. 6 and 7. It is very likely that there is more high-frequency structure associated with the propagation of a streamer than was evident on the instrumentation available at that time. The spectrum out to frequencies of roughly 10 MHz is adequately represented by the existing data.

## V CONCLUSIONS AND RECOMMENDATIONS

The objectives of the present program were to employ existing information regarding precipitation-static noise generation and coupling processes to develop a computer model that could be incorporated into the Intrasystem EMC analysis program. Such a model was generated, and tested by comparing its predictions with flight-test data generated on earlier p-static research programs. Within the limits of existing data, it was possible to predict with good accuracy the precipitation-static noise levels to be expected in flight.

The computer program includes provisions for suppressing the noise from one or more of the various sources to permit the EMC engineer to investigate the importance of applying noise-reduction measures to each of the sources. This capability is important because implementing noise-reduction techniques on certain parts of the aircraft may be costly, whereas in other areas they can be implemented with ease. Thus, the EMC engineer is always in the position of having to defend the necessity for carrying out all of his noise-reduction recommendations.

In preparing the computer model, every effort was made to incorporate the maximum flexibility commensurate with avoiding undue complexity. An effort was made to recognize areas where growth of the model should be expected, and to provide for the possibility of future expansion in these areas.

To use the resulting computer model, the EMC engineer must prepare a set of input cards describing the aircraft, and its speed, altitude regime, location of receiving "antennas", etc. The output of the program

provides information regarding the total charging current to the aircraft together with the magnitudes of the noise fields at the locations of interest as well as the magnitudes of the short-circuit currents induced in antennas of specified induction area at these locations. In general, these outputs are adequate to specify the noise environment sufficiently to permit judgements regarding the functioning of avionic systems and regarding the need for fixes.

As was recognized at the outset, the computer model is limited by the available technological base. This became more apparent as development of the computer model progressed. In particular there is a need for more information on noise coupling. It is important to be able to specify the coupling to more than two general regions on a particular aircraft. Of even greater importance, the coupling data need to be extended to other vehicle types. These should include a wide variety of aircraft types as well as rockets, helicopters, etc.

The increasing importance of digital avionics systems indicates that attention should be given to their susceptibility to individual noise pulses. The present coupling data do not contain information about the phase of the coupling function, so that it is not possible to predict the structure of individual p-static noise pulses coupled into systems. In future work to generate coupling data, the scheme used should include the capability of providing phase information.

The coupling data base can be enlarged either by experimental measurements or by computational means. Recent developments in both instrumentation and computer methods offer considerable promise in this regard. Ideally, one should provide for both analytical as well as experimental work, to generate faith in the results.

On the present program an effort was made to investigate the feasibility of using computational techniques such as the method of

moments to generate coupling data. The very crude model used was remarkably accurate in predicting the form and magnitude of the coupling between the tail-cap antenna region and a noise source on an elevator tip on the KC-135 aircraft. These techniques should definitely be exploited further, since they provide phase as well as amplitude information as a matter of course.

The process of preparing the computer model served to reemphasize the fact that the basic p-static noise-source data are based on measurements made up to 20 years ago, and are consequently limited by the instrumentation available at that time as well as by the investigator's view of what was required. In particular, limits on available instrumentation made it difficult to define the character of the noise sources above 10 to 20 MHz. This was not considered a limitation at that time because VHF systems were operated at relatively high signal levels. Also, microwave system design was such that it was quite impervious to p-static interference. At present, with satellite communication systems being considered for aircraft, it will be necessary for VHF systems to operate at substantially lower signal levels, so that VHF components of p-static noise may be significant. For these reasons, the noise-source data should be examined using modern instrumentation.

In view of the increased use of dielectric materials in aircraft construction, a careful review should be made of the streamer noise problem. The spectral data in this area are based on the most primitive of the p-static flight-test measurements.

A further consequence of the increased use of composite materials is that the electromagnetic shielding provided by metal skin will no longer exist. This result is immediately recognized in the case of frontal dielectric surfaces exposed to precipitation charging and the consequent streamering. If large regions of dielectric are incorporated into the design, however, the reduced shielding may also manifest itself

in increased susceptibility to corona noise. The consequences of such reduced shielding must be assessed.

Whenever possible, the future work should include provisions for flight-test verification of the results. Such testing is essential to provide confidence in the analytical and laboratory experimental results, as well as an opportunity to uncover unexpected effects. Ideally, the aircraft selected for the tests should include as many as possible of the materials and systems recognized to lead to p-static susceptibility. These should include composite surfaces, and, particularly avionics systems employing digital subsystems and computers operating with low-level signals. The tests should include measurements of noise source characteristics using modern instrumentation, and monitoring of the functioning and susceptibility of the aircraft's avionics systems.

Appendix A

STREAMER DISCHARGE CHARACTERISTICS

Appendix A

STREAMER DISCHARGE CHARACTERISTICS

1. General

In Ref. 7 the results of laboratory work, flight test measurements on a B-4 aircraft, and theoretical analysis are combined on page 47 to yield an expression for the short-circuit current induced in a receiving antenna by the occurrence of a streamer discharge on a plastic surface. The result [Eq. (26) of Ref. 7] is

$$I_1^{II}(t) = I_m \psi \left\{ \left[ \frac{a}{\alpha} (1 - e^{-\alpha t}) + \frac{b}{\beta} (1 - e^{-\beta t}) \right] u(t) - \left[ \frac{a}{\alpha} \left( 1 - e^{-\alpha \left( t - \frac{\ell}{v} \right)} \right) + \frac{b}{\beta} \left( 1 - e^{-\beta \left( t - \frac{\ell}{v} \right)} \right) \right] u \left( t - \frac{\ell}{v} \right) \right\} \quad (A-1)$$

where  $u(z)$  is the unit step defined by

$$u(z) = 0 \quad \text{for } z < 0$$

$$u(z) = 1 \quad \text{for } z > 0,$$

$\psi$  defines the electromagnetic coupling between the streamer source and the receiving system, and

$$I_m, a, b, \alpha, \beta, \ell, v$$

are all characteristics of the streamer breakdown itself. The values of  $l$  and  $v$  are as follows:

$l$  = Streamer length

$v$  = Streamer velocity =  $1.27 \times 10^5$  m/s.

and the remainder are obtained from the expression for the current flowing past a point in the streamer discharge packet [Eq. (21) of Ref. 7], reproduced here:

$$r_2^{II}(s_1, t) = I_{\max} \left( a e^{-\alpha t} + b e^{-\beta t} \right) \quad (\text{A-2})$$

where, for a typical streamer,

$a = 0.597$

$b = 0.403$

$\alpha = 1.67 \times 10^7 \text{ s}^{-1}$

$\beta = 5.47 \times 10^6 \text{ s}^{-1}$

$I_m = 0.01 \text{ A.}$

Equation (A-2) was evaluated for a typical value of coupling factor,  $\psi = 3 \text{ m}^{-1}$  (typical for a wire located immediately below the streamer), and for several streamer lengths, and the results plotted in Figure 4 (Section II-B). Although the time waveform of individual noise pulses induced by streamer discharges is of interest, it is necessary to be able to express the results in terms of the noise spectrum generated by a series of these pulses occurring at random times with varying discharge lengths and appropriately differing amplitudes. Such a calculation was carried out in Ref. 7, and numerical results were obtained for the case of streamers occurring on a triangular-shaped radome section directly over an antenna wire. (In this case,  $\psi$  and  $l$  both varied from discharge to discharge.)

The general expression for the short-circuit current noise-power spectrum induced in an antenna by a series of streamer pulses is given by:

$$G(\omega) = \frac{\nu I_m^2 \nu^2}{\pi} |g(\omega)|^2 \overline{|f(x, \ell)|^2} \quad (\text{A-3})$$

where, as before,  $I_m$  is the peak value of the current flowing in the discharge,  $\nu$  is the velocity of propagation of the discharge, and  $\nu$  is the average rate of occurrence of the streamers. The term  $|g(\omega)|^2$  is the square of the Fourier transform of the basic function

$$\frac{a}{\alpha} \left(1 - e^{-\alpha t}\right) + \frac{b}{\beta} \left(1 - e^{-\beta t}\right) \quad (\text{A-4})$$

used in describing the pulse produced by an average streamer [see Eq. (A-1)] and is given by

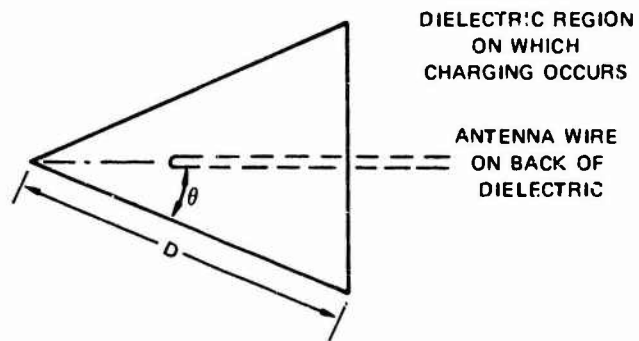
$$|g(\omega)|^2 = \frac{1}{\nu} \frac{(a+b)^2 + (a\beta + b\alpha)^2}{(\alpha^2 + \omega^2)(\beta^2 + \omega^2)} \quad (\text{A-5})$$

where the parameters are defined as in Eq. (A-2). The term  $\overline{|f(x, \ell)|^2}$  in eq. (A-3) is the ensemble average of the function

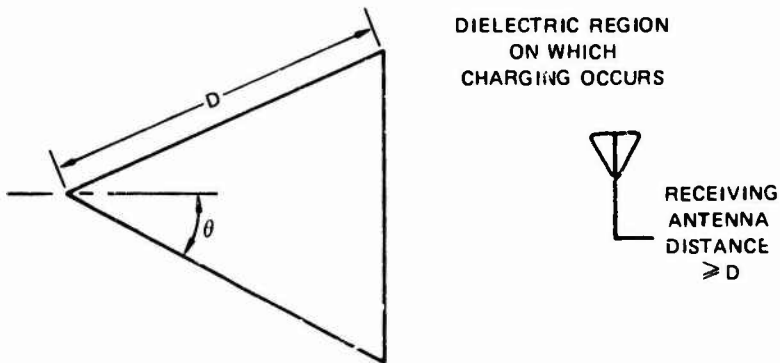
$$f \left( x_{\hat{h}}, \ell_{\hat{h}} \right) = \psi \left( x_{\hat{h}} \right) \left[ 1 - e^{-j(I/\nu)\ell_{\hat{h}}} \right] \quad (\text{A-6})$$

over the random variables  $x_{\hat{h}}$  and  $\ell_{\hat{h}}$ , and defines the statistics of the discharges occurring on a particular surface.

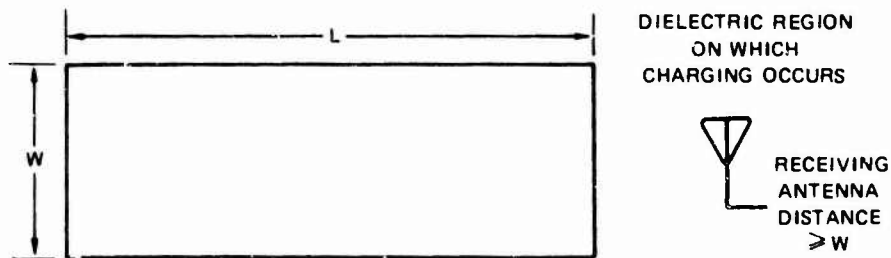
To perform the indicated averaging, it will be necessary to know the probability density  $h_1(\ell, x)$  of a discharge of length  $\ell$  originating



(a) TRIANGULAR DIELECTRIC, ANTENNA WIRE ON BACK



(b) TRIANGULAR DIELECTRIC, ANTENNA DISTANT



(c) RECTANGULAR DIELECTRIC, ANTENNA DISTANT

SA-2919-22

FIGURE A-1 DIELECTRIC SHAPES AND ANTENNA ARRANGEMENTS FOR WHICH STREAMER STATISTICAL CALCULATIONS WERE CARRIED OUT

from the point  $x$  on the rim around the charged dielectric region. These statistics may be inferred from the manner in which the dielectric surface becomes charged. Such an evaluation was carried out in Ref. 7 for a special radome used on the B-47 flight-test aircraft. The calculations of Ref. 7 will be reproduced here and will be extended to other geometries of interest so that ultimately we will have expressions for the three combinations of dielectric surface and antenna location illustrated in Figure A-1. The arrangements shown in the figure were chosen because they represent the range of charging situations and antenna arrangements one is likely to encounter in practice. Figures A-1(a) and (b) are typical of the charging and breakdown situation one would have either on a fighter windshield or on a radome equipped with lightning-diverter strips. The shape of Figure A-1(c) corresponds to a dielectric region located on the leading surface of an airfoil.

The arrangement of Figure A-1(a) is representative of an "antenna" located immediately below the dielectric surface on which charging and streamers occur. Figures A-1(b) and (c) are representative of situations in which the antenna element is not immediately adjacent to the dielectric surface on which streamering is occurring.

## 2. Evaluation of Streamer Statistics

### a. Triangular Dielectric Over Antenna Wire

In the flight tests of Ref. 7, a special nose consisting of four triangular-shaped radome sections was installed on the nose of the B-47 flight-test aircraft. For purposes of this analysis it will be convenient to approximate the radome section by a plane triangle and to assume that all of the charging of the radome section occurred in the unshaded region shown in Figure A-2. Another assumption that will be made at this time is that the entire unshaded region of Figure A-2

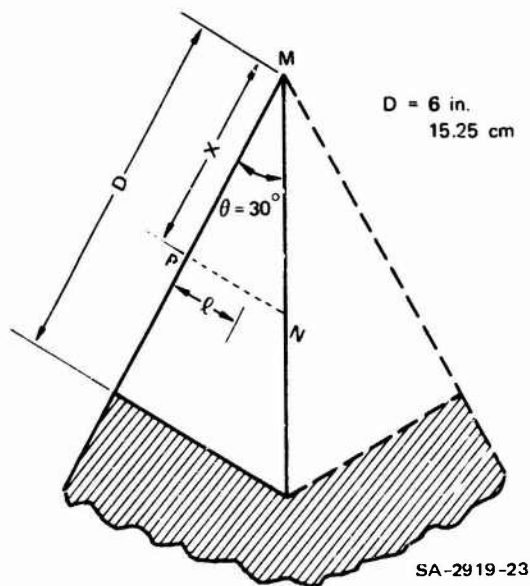


FIGURE A-2 APPROXIMATION TO REGION OF RADOME IN WHICH CHARGING OCCURRED

charged at a uniform rate. Although the charging rate of the radome surface did vary with distance,  $x$ , from the nose of the radome, the evaluation of this variation is a lengthy aerodynamic problem. Since very little is known regarding the aerodynamic properties of ice crystals, the results of the aerodynamic calculation would only be of a qualitative nature. Thus it was felt that the increased accuracy that might result from including the variation of charging rate in the present calculations was not worth the additional effort.

Since it has been assumed that the unshaded region of Figure A-2 charges at a uniform rate, the probability of a discharge occurring from a point  $0 < x < x$  [written  $P(0 < x < x)$ ] is proportional to the area

$$a = \frac{1}{2} x(x \tan \theta) \tag{A-7}$$

enclosed by the triangle MNP shown in the figure. The total area in which charging occurs is given by

$$A = \frac{1}{2}D^2 \tan \theta \quad . \quad (A-8)$$

Thus,

$$\begin{aligned} P(0 < X < x) &= \frac{a}{A} = \frac{x^2}{D^2} & 0 < x < D \\ &= 0 & \text{elsewhere.} \end{aligned}$$

The probability density  $h_3(x)$  of a discharge from a point  $x$  along the rim is, therefore,

$$\begin{aligned} h_3(x) &= \frac{dP}{dx} = \frac{2x}{D} & 0 < x < D \\ &= 0 & \text{elsewhere.} \end{aligned} \quad (A-9)$$

Given that the discharge occurs from the point  $\cdot$  a discharge extending to any point on the line PN in Figure A-2 is equally likely since it has been assumed that the entire surface charges at a uniform rate. Thus the conditional probability density of a discharge of length  $\ell$  [written  $h_2(\ell|x)$ ] is given by the rectangular density function

$$\begin{aligned} h_2(\ell|x) &= \frac{1}{x \tan \theta} & 0 < \ell < x \tan \theta \\ &= 0 & \text{elsewhere.} \end{aligned} \quad (A-10)$$

The joint density function  $h_1(\ell, x)$  is given by

$$h_1(\ell, x) = h_2(\ell|x)h_3(x)$$

which, upon substituting Eqs. (A-9) and (A-10), becomes

$$h_1(\ell, x) = \frac{2}{D^2 \tan \theta} .$$

Letting  $\gamma = \tan \theta$ , we obtain

$$\begin{aligned} h_1(\ell, x) &= \frac{2}{D^2 \gamma} && 0 < \ell < \gamma x \\ & && 0 < x < D \\ &= 0 && \text{elsewhere.} \end{aligned} \tag{A-11}$$

With the above information available, we may now evaluate  $\overline{|f(x, \ell)|^2}$ .

Reproducing Eq. (A-6),

$$f(x, \ell) = \psi(x) \left( 1 - e^{-j(\omega/v)\ell} \right), \tag{A-6}$$

we may write

$$|f(x, \ell)|^2 = \psi^2(x) \left( 1 - e^{-j(\omega/v)\ell} \right) \left( 1 - e^{j(\omega/v)\ell} \right)$$

which becomes

$$|f(x, \ell)|^2 = 2\psi^2(x) \left( 1 - \cos \frac{\omega}{v} \ell \right) . \tag{A-12}$$

The ensemble average over the random variables  $x$  and  $\ell$  is given by

$$\overline{|f(x, \ell)|^2} = \int_{\ell=0}^{\gamma x} \int_{x=0}^D |f(x, \ell)|^2 h_1(\ell, x) dx d\ell .$$

Substituting Eqs. (A-12) and (A-11) we obtain

$$\overline{|f(x, \ell)|^2} = \frac{4}{D^2} \int_{\ell=0}^{\gamma x} \int_{x=0}^D \psi^2(x) \left( 1 - \cos \frac{\omega}{v} \ell \right) dx d\ell .$$

The integration with respect to  $\ell$  may be performed immediately to give

$$\overline{|f(x, \ell)|^2} = \frac{4}{D^2} \int_0^D \psi^2(x) \left( x - \frac{v}{\omega} \sin \frac{\omega v}{v} x \right) dx . \quad (A-13)$$

It will now be necessary to obtain an expression for  $\psi(x)$ . The measured values of  $\psi$  one centimeter in from the rim in Ref. 7 are shown plotted versus  $x$  in Figure A-3. It is evident from the figure that the points lie very nearly along the straight line.  $\psi = mx$  where  $m = 32 \text{ m}^{-2}$ .

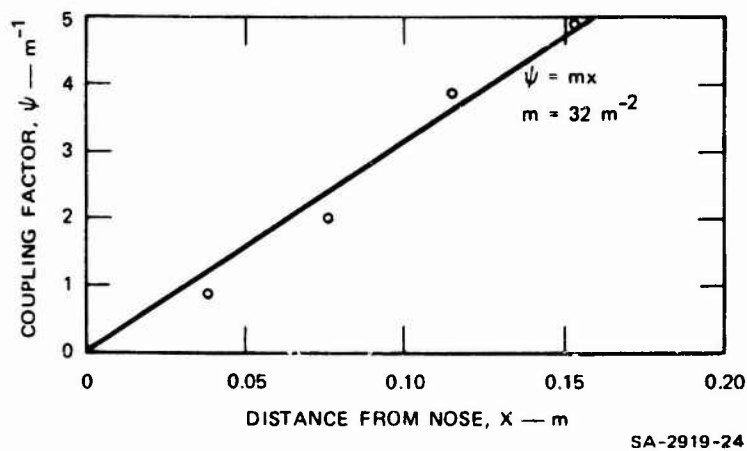


FIGURE A-3 VARIATION OF COUPLING FACTOR WITH DISTANCE FROM RADOME NOSE

Substituting the above expression for  $\psi(x)$  into Eq. (A-13)

gives

$$\overline{|f(x, \ell)|^2} = \frac{4m^2}{D^2} \int_0^D x^2 \left( x - \frac{v}{\omega} \sin \frac{\omega v}{v} x \right) dx . \quad (A-14)$$

Upon performing the indicated integration and rearranging terms, Eq. (A-14) becomes

$$\overline{|f(x, \ell)|^2} = 4m^2 \left\{ \frac{D^2}{4} + \frac{v^2}{\gamma^2 \omega^2} \left[ \left( \frac{\sin \frac{\gamma D}{2v} \omega}{\frac{\gamma D}{2v} \omega} \right)^2 + \cos \frac{\gamma D}{v} \omega - 2 \frac{\sin \frac{\gamma D}{v} \omega}{\frac{\gamma D}{v} \omega} \right] \right\} \quad (\text{A-15})$$

b. Triangular Dielectric, Distant Antenna

Since we are considering a dielectric surface that has the same shape and exposure to precipitation as in Section 2-a, above, the arguments regarding the statistics of streamer discharge location and length will be unchanged. Thus, we may simply start with Eq. (A-13), and modify the succeeding steps as appropriate for the different antenna coupling.

Because the receiving antenna is not in the immediate vicinity of the dielectric surface and surrounding rim, the coupling  $\psi$  will be far less sensitive to position than it was in the previous analysis. Let us assume, in fact, that the coupling is constant and independent of  $x$  in Figure A-2. Substituting into Eq. (A-13) we obtain

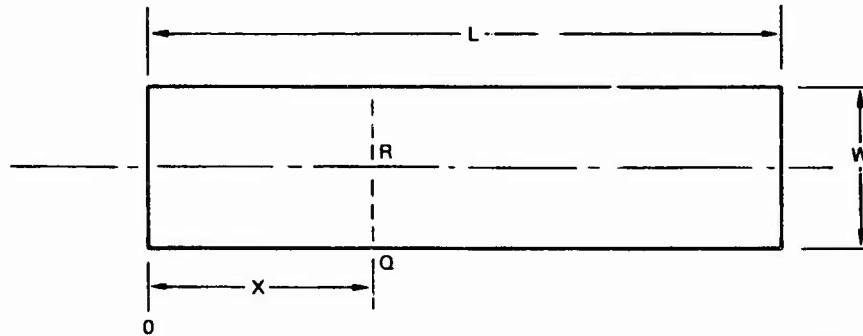
$$\overline{|f(x, \ell)|^2} = \frac{4\psi^2}{D^2} \int_0^D \left( x - \frac{v}{\omega\psi} \sin \frac{\omega\gamma}{v} x \right) dx. \quad (\text{A-16})$$

Upon performing the integration and rearranging, Eq. (A-16) becomes

$$\overline{|f(x, \ell)|^2} = 2\psi^2 \left[ 1 - \left( \frac{\sin \frac{\gamma D}{2v} \omega}{\frac{\gamma D}{2v} \omega} \right)^2 \right]. \quad (\text{A-17})$$

c. Rectangular Dielectric, Distant Antenna

Let us now consider the case of a rectangular dielectric region as illustrated in Figure A-4 undergoing uniform charging. The probability



SA-2919-25

FIGURE A-4 RECTANGULAR DIELECTRIC REGION OF CHARGING

of a discharge occurring from a point  $0 < x < L$  [written  $P(0 < x < L)$ ] is proportional to the area

$$a = Wx \quad (A-18)$$

enclosed by the rectangle to the left of the dotted line in the figure. The total area in which charging occurs is given by

$$A = LW \quad (A-19)$$

Thus,

$$\begin{aligned} P(0 < x < L) &= \frac{a}{A} \\ &= \frac{x}{L} \quad 0 < x < L \quad (A-20) \\ &= 0 \quad \text{elsewhere} . \end{aligned}$$

The probability density  $h_3(x)$  of a discharge from the point  $x$  along the rim is, therefore,

$$\begin{aligned}
h_3(x) &= \frac{dP}{dx} \\
&= \frac{1}{L} & 0 < x < L \\
&= 0 & \text{elsewhere} .
\end{aligned}
\tag{A-21}$$

Given that the discharge occurs from the point  $x$ , a discharge extending to any point along the line QR is equally likely, since it has been assumed that the entire surface charges at a uniform rate. Thus, the conditional probability density of a discharge of length  $l$  [written  $h_2(l|x)$ ] is given by the rectangular density function

$$\begin{aligned}
h_2(l|x) &= \frac{2}{W} & 0 < l < \frac{W}{2} \\
&= 0 & \text{elsewhere} .
\end{aligned}
\tag{A-22}$$

The joint density function  $h_1(l, x)$  is given by

$$\begin{aligned}
h_1(l, x) &= h_2(l|x) h_3(x) \\
&= \frac{2}{W} \frac{1}{L} \\
&= \frac{2}{LW} & \text{for } 0 < l < \frac{W}{2} \\
& & 0 < x < L .
\end{aligned}
\tag{A-23}$$

Picking up the argument at Eq. (A-12)

$$|f(x, l)|^2 = 2v^2(x) \left(1 - \cos \frac{w}{v} l\right) .
\tag{A-12}$$

The ensemble average over the random variables  $x$  and  $l$  is given by

$$\overline{|f(x, \ell)|^2} = \int_{\ell=0}^{W/2} \int_{x=0}^L |f(x, \ell)|^2 h_1(\ell, x) dx d\ell. \quad (A-24)$$

Substituting Eqs. (A-12) and (A-23) into Eq. (A-24),

$$\overline{|f(x, \ell)|^2} = \frac{2}{LW} \int_{\ell=0}^{W/2} \int_{x=0}^L 2\psi^2(x) \left(1 - \cos \frac{\omega}{v} \ell\right) dx d\ell. \quad (A-25)$$

Integrating with respect to  $\ell$  gives

$$\overline{|f(x, \ell)|^2} = \frac{4}{LW} \int_0^L \psi^2(x) \left(\frac{W}{2} - \frac{v}{\omega} \sin \frac{\omega}{v} \frac{W}{2}\right) dx. \quad (A-26)$$

As in the previous section, let us say that the antenna is removed to a distance large compared to  $W$  from the charged dielectric surface on which streamers are occurring, and that  $\psi$  is constant over the dielectric.

With this restriction, Eq. (A-26) becomes

$$\overline{|f(x, \ell)|^2} = \frac{4\psi^2}{LW} \int_0^L \left(\frac{W}{2} - \frac{v}{\omega} \sin \frac{\omega W}{2v}\right) dx \quad (A-27)$$

which, upon integration and simplification, becomes

$$\overline{|f(x, \ell)|^2} = 2\psi^2 \left[ 1 - \frac{\sin \frac{W}{2v} \omega}{\frac{W}{2v} \omega} \right]. \quad (A-28)$$

### 3. Streamer-Noise-Source Spectra

The results of the statistical analyses of streamers are given in Table A-1. A simple presentation of formulas in a table provides little insight into the way streamer noise characteristics are affected by the

significant physical changes considered in the analysis. Accordingly, Eq. (A-3) was evaluated for the three geometries considered in Figure A-1 and Table A-1 for charging conditions such that the total dc current

Table A-1

RESULTS OF STREAMER STATISTICAL CALCULATIONS

Physical Arrangement	$ f(x, l) ^2$
Figure A-1(a)	$4m^2 \left\{ \frac{D^2}{4} + \frac{v^2}{2\omega^2} \left[ \left( \frac{\sin \frac{\gamma D}{2v} \omega \right)^2 + \cos \frac{\gamma D}{v} \omega - 2 \frac{\sin \frac{\gamma D}{v} \omega}{\frac{\gamma D}{v} \omega} \right] \right\}$
Figure A-1(b)	$2\psi^2 \left[ 1 - \left( \frac{\sin \frac{\gamma D}{2v} \omega}{\frac{\gamma D}{2v}} \right)^2 \right]$
Figure A-1(c)	$2\psi^2 \left[ 1 - \frac{\sin \frac{W}{2v} \omega}{\frac{W}{2v} \omega} \right]$

discharged by streamers is  $I_{dc} = 1 \mu A$ , which corresponds to a streamer PRF  $\nu = 666 \text{ s}^{-1}$ . The values chosen for the other parameters are as follows:

$$\psi = 1 \text{ m}^{-1}$$

$$m = 10.6 \text{ m}^{-2}$$

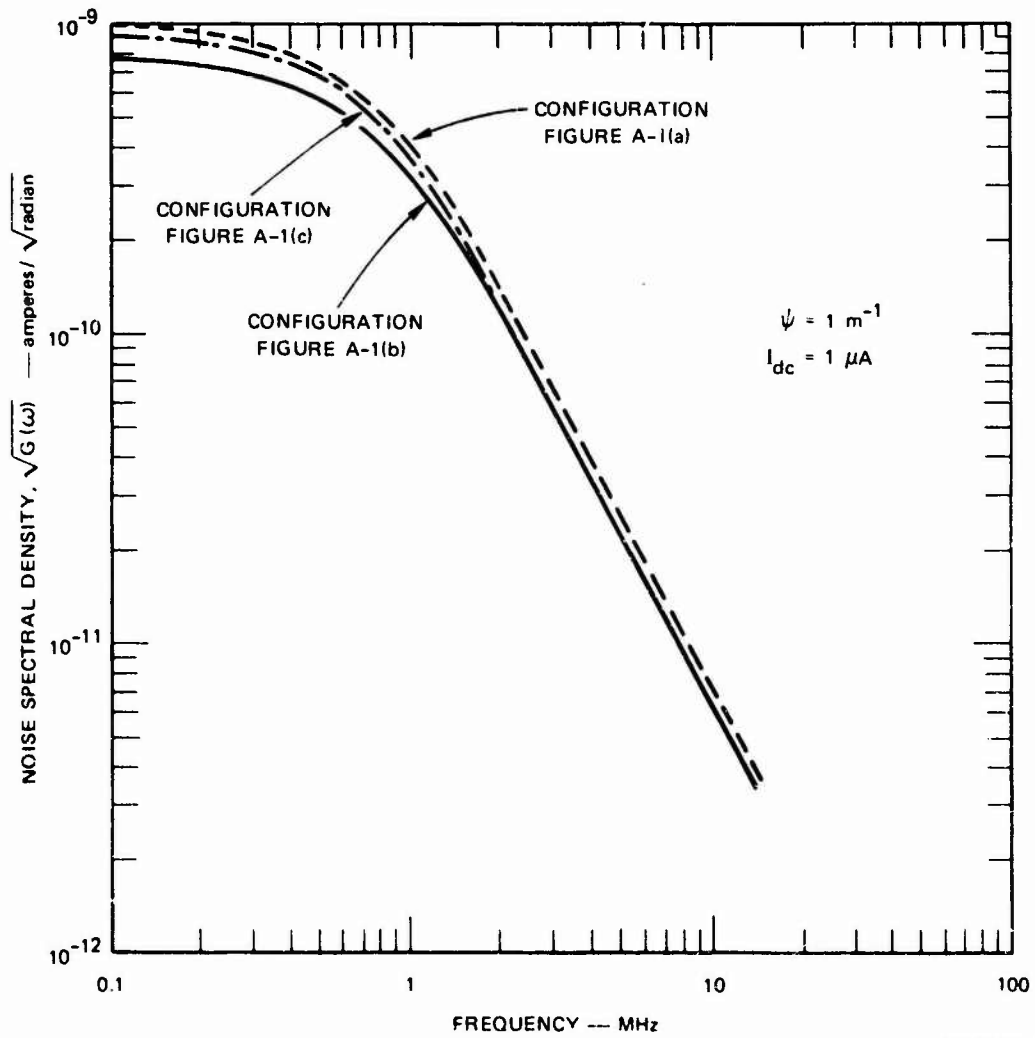
$$D = 0.15 \text{ m}$$

$$\gamma = \tan \theta = 0.58$$

$$W = 0.15 \text{ m.}$$

Since  $\psi = 1$  and  $I = 1 \text{ } \mu\text{A}$ , the data are in effect normalized to unity coupling and unity streamer discharge current. (To apply the data to other charging and coupling conditions it should be borne in mind that the noise spectral density varies directly with the coupling factor  $\psi$  and as  $\sqrt{I_{\text{dc}}}$ .) The selected parameter values correspond to the range of the physical dimensions and couplings for the nose radome used in the B-47 flight tests of Ref. 7, as illustrated in Figure A-1(a). The resulting noise spectra are shown in Figure A-5. It is evident that in spite of the great disparity in the formulations of  $|f(x, \ell)|^2$  in Table A-1 the three spectra are almost identical in the frequency range considered. This result is significant in that it means that details of the geometry of the dielectric region and details of antenna location do not noticeably affect the form or magnitude of the resulting noise spectrum. Thus, we can be quite loose in defining the precise streamer geometry and still obtain valid noise data.

To further explore the effects on the noise spectrum of varying streamer geometry, calculations were carried out to determine the noise spectra generated by a given charging current ( $I_{\text{dc}} = 1 \text{ } \mu\text{A}$ ,  $v = 666 \text{ s}^{-1}$ ) on regions of a given shape but of varying size. The results of such calculations for a triangular region are shown in Figure A-6 and for a rectangular region in Figure A-7. It is evident from these two figures that increasing the size of the region (this increases streamer length) has the effect of increasing the low-frequency content of the noise spectrum. This is in keeping with the results shown in Figure 4 where it is indicated that increasing the length of the streamers has the effect of stretching the induced-current pulse, thereby increasing its low-frequency content.



SA 2919-26

FIGURE A-5 STREAMER-NOISE-SOURCE SPECTRA FOR THE PHYSICAL CONFIGURATION OF FIGURE A-1

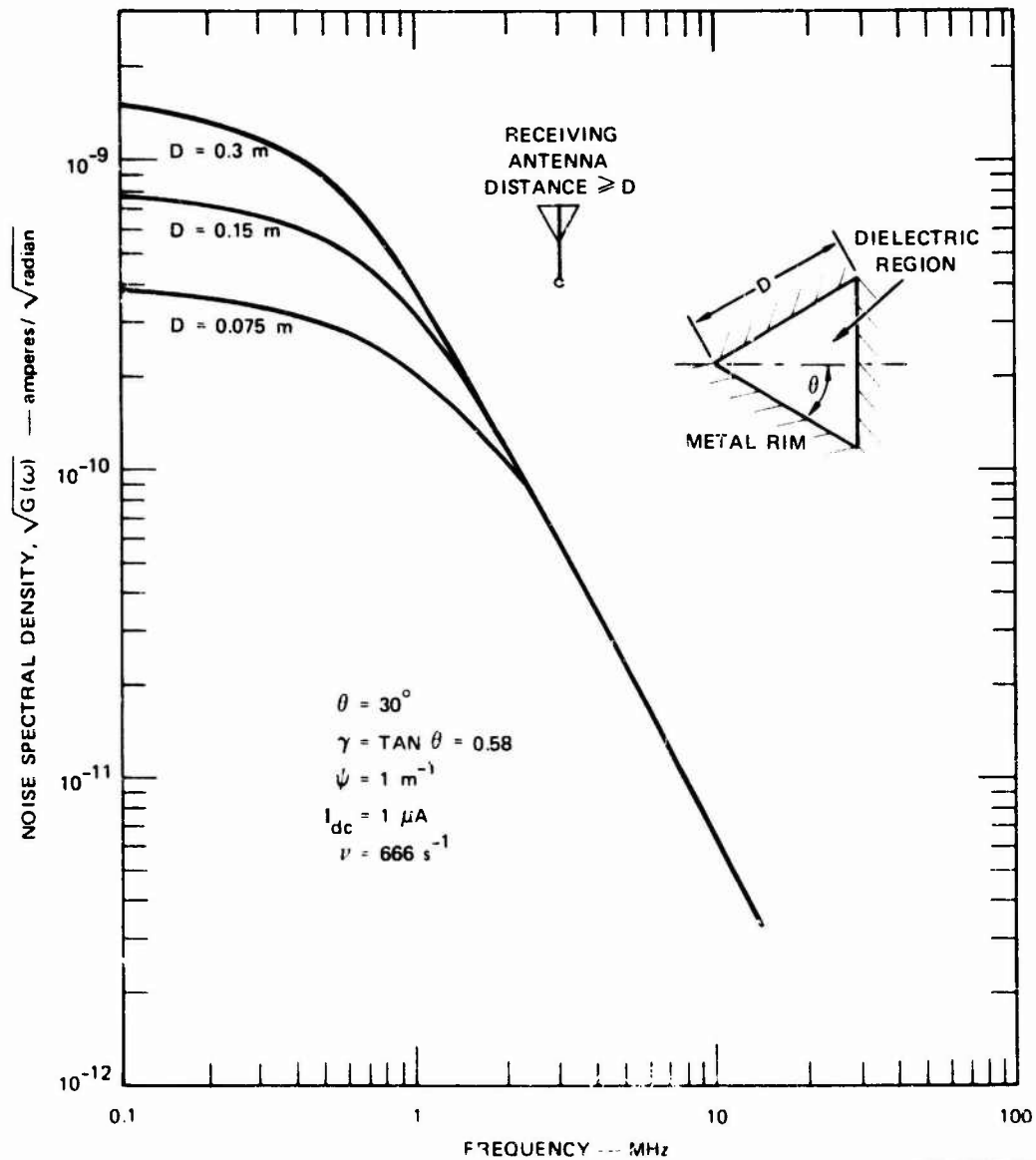


FIGURE A-6 STREAMER-NOISE-SOURCE SPECTRA FOR TRIANGULAR DIELECTRIC REGIONS

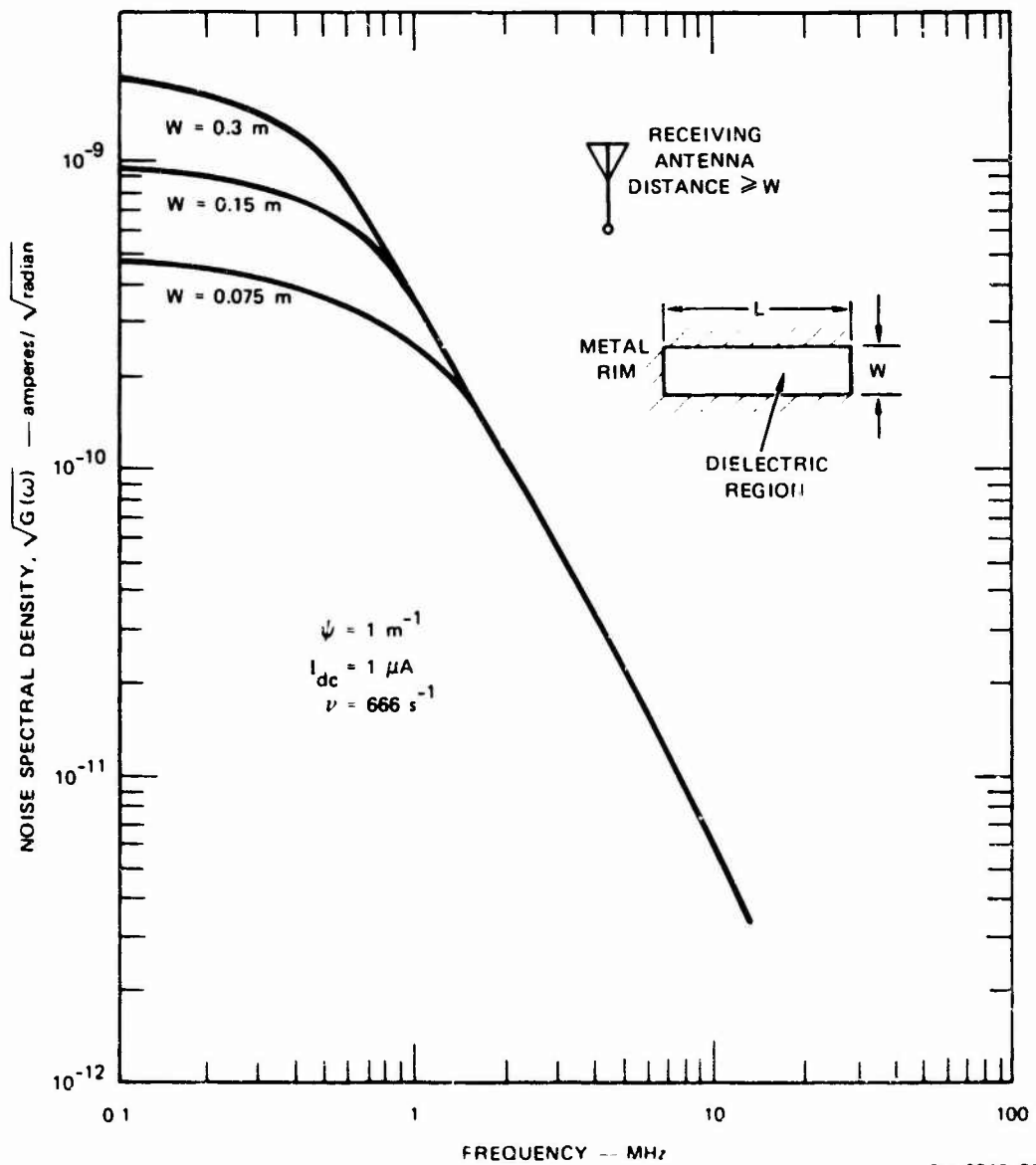


FIGURE A-7 STREAMER-NOISE-SOURCE SPECTRA FOR RECTANGULAR DIELECTRIC REGIONS

Appendix B

METHOD-OF-MOMENTS CALCULATION OF COUPLING TO KC-135 TAIL-CAP

## Appendix B

### METHOD-OF-MOMENTS CALCULATION OF COUPLING TO KC-135 TAIL-CAP

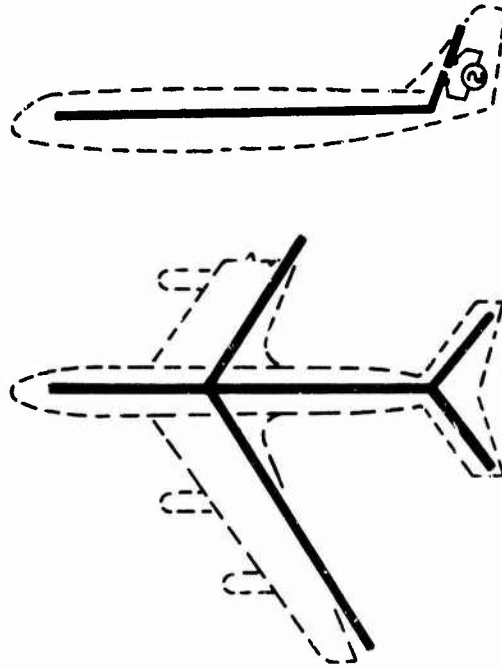
#### 1. General

In connection with SRI's general internal development and upgrading of techniques for the solution of electromagnetic problems, two method-of-moments computer codes were being investigated concurrently with the program reported here, for use on the SRI CDC 6400 digital computer. One of these codes was debugged and successfully running shortly before the end of the present research program. This code was capable of solving for the currents and fields in the vicinity of a structure made up of a limited number of cylindrical elements. Discussions with the personnel involved with the internal SRI research program indicated that the computer code they had prepared could be used very simply to carry out a preliminary calculation to investigate the feasibility of employing computer methods to determine the electromagnetic coupling between noise sources and antennas on aircraft. Accordingly, provisions were made on the present program to approximate the KC-135 aircraft by a series of cylinders and to carry out the calculation of the coupling between the tail-cap antenna and the wing-tip and elevator-tip regions.

It was recognized that the approximation would be very crude, and that precise agreement of numerical magnitudes of the computed couplings with measured data would be fortuitous. It was felt, however, that the degree of agreement between measured and computed resonances would be indication of the ultimate workability of the analytical method.

## 2. Coupling Calculation

For the calculation, the KC-135 aircraft was approximated by the structure of 0.5-m-diameter cylinders shown in Figure B-1. It is



SA-2919-29

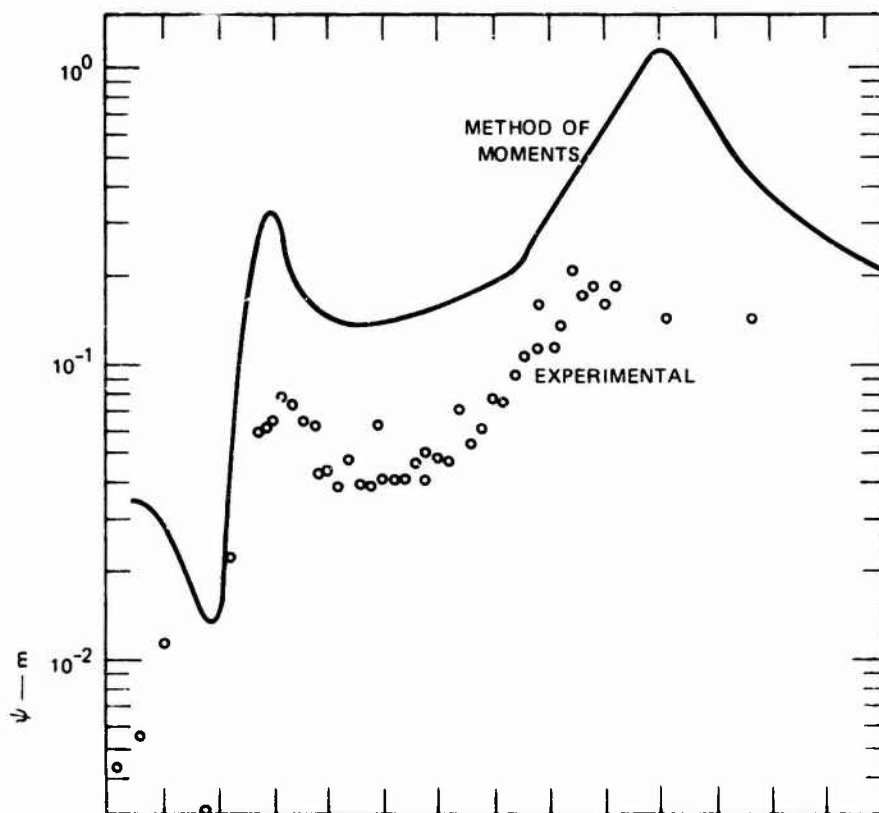
FIGURE B-1 CYLINDRICAL ELEMENT APPROXIMATION TO KC-135 AIRCRAFT

evident that such a mathematical model approximates only the grossest features of the aircraft. For example, the wings and empennage structures attach to the proper positions on the aircraft fuselage, and are oriented at the correct angle to the fuselage, but the cylinder diameter is generally not properly scaled. In particular, no effort is made to scale the taper of the airfoils. The modeling was deliberately made this simple in order to restrict computer requirements to manageable levels. The restrictions on the modeling, of course, mean that although the gross currents on the aircraft may be accurately modeled, one should not expect accurate estimates of currents and fields near the tips of the airfoil extremities.

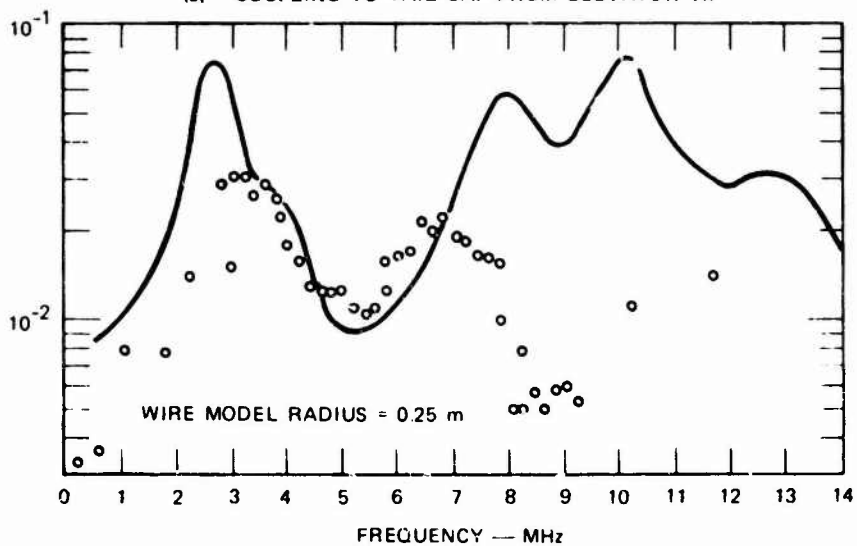
The way in which the tail-cap antenna was modeled is also evident in Figure B-1. The top half of the vertical fin was considered to be isolated from the aircraft and driven by a 1-volt generator. Obviously the size of such an antenna is much larger than that actually used on the KC-135 aircraft, so we should expect the calculated coupling fields to be higher than the measured ones.

Calculations were made of the currents flowing on the various members and the fields in their vicinity as the result of the 1-volt excitation of the antenna. Of most interest here is the magnitude of the electric field in the vicinity of the airfoil tips. Calculations were made of the field intensity 0.5 m inboard from the "airfoil" tip, and 0.01 r above the surface. The magnitude of this normalized field is by definition the magnitude of the coupling to this point,  $\psi = E/V$ , as defined in Section II-C of the main text. The results of the airfoil-tip field calculations are shown in Figure B-2 along with experimentally measured data points from the corona coupling studies of Ref. 4. It should be noted that for both the wing-tip and the elevator tip, the magnitudes of the coupling are in remarkably good agreement if one considers the fact that no effort was made to accurately model the details of either the antenna or the airfoil tips.

To better show the degree to which the computation accurately predicted aircraft resonances, the magnitudes of the calculated couplings were adjusted in Figure B-3 for best fit to the experimental data. In Figure B-3(a), the calculated coupling curve duplicates the measured resonances with remarkable precision. Particularly significant is the coupling minimum at  $f = 2$  MHz predicted by the calculations. When the experimental data were first obtained in the work of Ref. 4, it was not clear whether the coupling minimum at  $f = 2$  MHz should be considered as being real, or whether it should be construed as a bad data point. When the data were presented (see Figure 10 of the present report), the



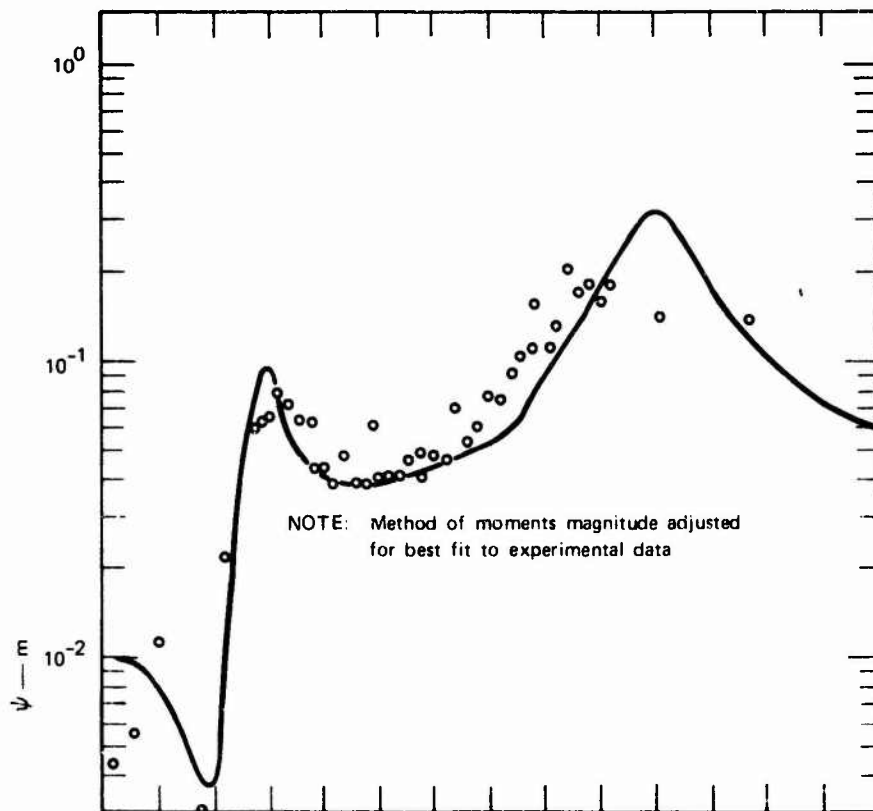
(a) COUPLING TO TAIL CAP FROM ELEVATOR TIP



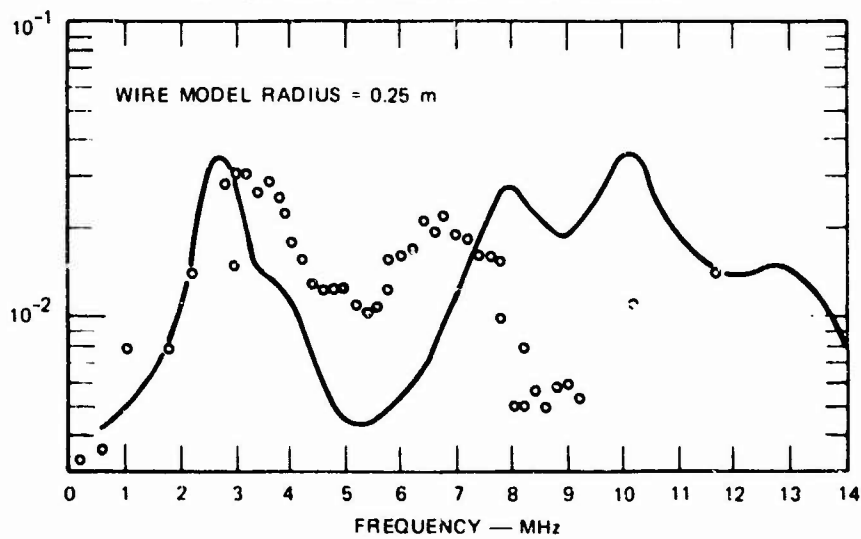
(b) COUPLING TO TAIL CAP FROM WING TIP

SA 2919-30

FIGURE B-2 COMPUTED AND EXPERIMENTAL COUPLING DATA



(a) COUPLING TO TAIL CAP FROM ELEVATOR TIP



(b) COUPLING FROM TAIL CAP TO WING TIP

SA-2919-31

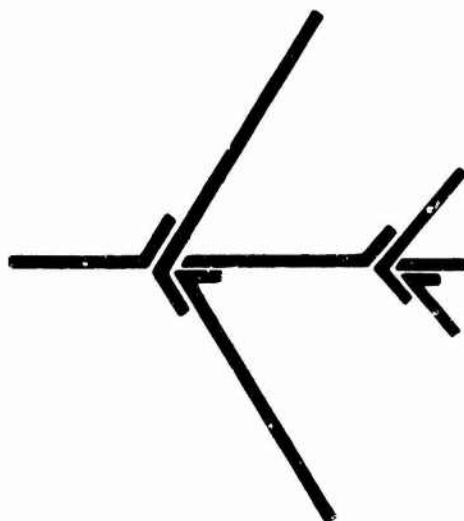
FIGURE B-3 ADJUSTED CALCULATIONS COMPARED TO MEASURED COUPLING DATA

minimum was treated as real. It is heartening that the rough computer calculations also indicate that the coupling minimum is real.

In Figure B-3(b) the agreement is good between calculated and experimental data at low frequencies. Above about  $f = 3\text{MHz}$ , this agreement gets progressively worse. The magnitudes of the coupling variations do not agree as well, and the frequencies of the maxima and minima disagree. Why the agreement is not better is not clear at this time. Intuitively, one would expect that the major resonances would be reproduced even with a model as crude as the one illustrated in Figure B-1. Unfortunately, time and funds did not permit experimentation with variation of parameters such as cylinder radius in the calculations in order to investigate the degree to which the accuracy of computer output is affected by the simplifications made in the mathematical modeling of the vehicle. Such checks and experiments are essential to final judgments regarding the viability of the computer method.

### 3. Brief Description of Method-of-Moments Computer Code Used

The basic computer code used for the method-of-moments calculations was patterned after that developed by Syracuse University for AFCRL and described in Ref. 19. To use this code, one must divide the structure under investigation into a series of cylinders that are constrained to run parallel to one another at the intersections as shown in Figure B-1. Each individual cylindrical conductor, in turn, is divided into a series of shorter cylindrical elements. Of course, the larger the number of cylinders and subelements one uses in describing the aircraft, the more accurate the simulation. Unfortunately, however, the computer core and time required to carry out the calculation varies roughly as the square of the number of elements employed. Thus, it is necessary to restrict the subdivision to the minimum number of elements adequate to produce the required detail in the output. Obviously, the degree of subdivision necessary increases as the highest frequency of interest is increased.



SA-2919-32

FIGURE B-4 TECHNIQUE FOR TREATING JOINTS IN METHOD-OF-MOMENTS CALCULATION

In the preliminary calculations performed on the present program, the aircraft was broken down into a total of 89 pieces. This made it possible to carry out the minimal calculations of the present program on the SRI CDC 6400 digital computer with 42,300<sub>8</sub> bits of the core memory of 150,000<sub>8</sub> bits. Once the program was debugged, it was found that this run required 61.6 s of computer time.

From the foregoing paragraph, it is evident that the method-of-moments calculation extended to more detailed configurations can tie up a large fraction of the total core of a computer. Accordingly, it is not clear that such a calculation should be made part of the Air Force Intrasytem EMC Analysis Program. It may be preferable to generate the coupling data separately for a number of typical configurations and simply read the data into PSTAT as was done here in connection with the experimentally generated coupling data of Figure 6.

#### ACKNOWLEDGMENT

The authors are grateful to Mr. S. Dairiki, also of SRI, who carried out the method-of-moments calculations discussed in Appendix B.

## REFERENCES

1. H. G. Hucke, "Precipitation Static Interference," Proc. IRE, Vol. 27, No. 5 (May 1939).
2. R. C. Ayers and J. O. Jarrard, "Aircraft Precipitation Static Investigation," Contract W 33-106 SC-70, Trans-World Airlines, Inc. (August 1944).
3. R. Gunn et al., "Army-Navy Precipitation Static Project," Proc. IRE, Vol. 34, Nos. 4 and 5 (1946).
4. R. L. Tanner and J. E. Nanevicz, "Precipitation Charging and Corona-Generated Interference in Aircraft," AFCRL 336, Tech. Report 73, Contract AF 19(604)-3458, SRI Project 2494, Stanford Research Institute, Menlo Park, Calif. (April 1961), AD-261 029.
5. R. L. Tanner and J. E. Nanevicz, "An Analysis of Corona-Generated Interference in Aircraft," Proc. IEEE, Vol. 52, No. 1, pp. 44-52 (January 1964).
6. R. L. Tanner and J. E. Nanevicz, "Radio Noise Generated on Aircraft Surfaces," Final Report, Contract AF 33(616)-2761, SRI Project 1267, Stanford Research Institute, Menlo Park, Calif. (September 1956).
7. J. E. Nanevicz, "A Study of Precipitation-Static Noise Generation in Aircraft Canopy Antennas," Tech. Report 62, Contract AF 19(604)-1296, SRI Project 1197, Stanford Research Institute, Menlo Park, Calif. (December 1957).
8. R. L. Tanner, "Radio Interference from Corona Discharges," Tech. Report 37, Contract AF 19(604)-266, SRI Project 591, Stanford Research Institute, Menlo Park, Calif. (April 1953).
9. A. L. Hiebert and S. A. Scharff, "An Electromagnetic Compatibility Program for the 1970's--Part I Intrasystem EMC Simulation, Analysis, and Control," WN-7256-1-PR, RAND Corporation, Santa Monica, Calif. (August 1971).

10. U.S. Standard Atmosphere, 1962, National Aeronautics and Space Administration, Washington, D.C. 20402.
11. J. E. Nanevich, E. F. Vance, W. C. Wadsworth, and J. A. Martin, "Low Altitude Long-Range All-Weather Vehicle Interference Investigation; Part I: Laboratory Studies," AFAL-TR-65-239, Part I, Contract AF 33(615)-1934, SRI Project 5082, Stanford Research Institute, Menlo Park, Calif. (August 1965).
12. A. Vassiliadis, "A Study of Corona Discharge Noise in Aircraft Antennas," Tech. Report 70, Contract AF 19(604)-3458, SRI Project 2494, Stanford Research Institute, Menlo Park, Calif. (July 1960).
13. J. T. Bolljahn and R. F. Reese, "Electrically Small Antennas and the Low-Frequency Aircraft Antenna Problem," IRE Trans., Vol. PGAP-1, No. 2 (October 1953).
14. J. E. Nanevich, Flight Evaluation of Induced-Noise Mechanisms on High-Speed Aircraft " AFAL-TR-73-317, Final Report, Contract F33615-68-C-1359, SRI Project 6091, Stanford Research Institute, Menlo Park, Calif. (October 1973).
15. R. J. Brun and R. G. Dorsch, "Impingement of Water Droplets on an Ellipsoid of Fineness Ratio 10 in Axisymmetric Flow," NACA Technical Note 3147, NACA, Washington, D.C. (May 1954).
16. R. G. Dorsch, R. J. Brun and J. L. Gregg, "Impingement of Water Droplets on an Ellipsoid of Fineness Ratio 5 in Axisymmetric Flow" NACA Technical Note 3099, NACA, Washington, D.C. (March 1954).
17. R. J. Brun, H. M. Gallegher, and D. C. Vogt, "Impingement of Water Droplets on NACA 65-208 and 65-212 Airfoils at 1 Angle of Attack," NACA Technical Note 2952, Washington, D.C. (May 1953).
18. A. G. Guibert, E. Janssen, and W. M. Robbins, "Determination of Rate, Area, and Distribution of Water Drops on Various Airfoils from Trajectories Obtained on the Differential Analyzer " NACA RM No. 9A05, University of California, Berkeley, Calif. (February 16, 1949).
19. D. C. Kuo, B. J. Strait, "Improved Programs for Analysis of Radiation and Scattering by Configurations of Arbitrarily Bent Thin Wires," AFRL-72-0051, Contract No. F19628-68-C-0180, Project No. 5635, Scientific Report No. 15, Department of Electrical and Computer Engineering, Syracuse University, Syracuse, N.Y. (January 1972).